FR-20424

FUNDAMENTAL UNDERSTANDING OF THE INTRINSIC DUCTILITY IN NICKEL-BASE $L1_2$ TYPE ALLOYS

C.C. Law, D.M. Shah, J. Lin
United Technologies Corporation
Pratt & Whitney Group
Government Engine Business
P.O. Box 2691
West Palm Beach, Florida 33402

June 1988

Final Report
Period 15 February 1986 Through 14 February 1988

Prepared for
Air Force Office of Scientific Research
Directorate of Electronic and Material Sciences
Building 410
Bolling AFB DC 20332-6448
Attn: Dr. Alan Rosenstein

UNITED TECHNOLOGIES

In reply please refer to
CCL:gla, MS 114-45
Ref. No. FR-20424

30 June 1988

To: Air Force Office of Scientific Research
Directorate of Electronic and Material Sciences
Building 410
Bolling AFB DC 20332-6448

Attention: Dr. Alan Rosenstein

Subject: Fundamental Understanding of the Intrinsic Ductility in Nickel-Base L1$_2$ Type Alloys - Final Report

Reference: Contract F49620-86-C-0033

Enclosures: Sixteen copies of the subject report, FR-20424

Gentlemen:

In accordance with terms of the reference contract, we herewith submit sixteen copies of the subject report.

Sincerely yours,

UNITED TECHNOLOGIES CORPORATION
Pratt & Whitney Group

C. C. Law
Program Manager

cc: Administrative Contracting Officer
Air Force Plant Representative Office
UTC/Pratt & Whitney Group
East Hartford, Connecticut 06108

A-1

Unclassified

SECURITY CLASSIFICATION OF THIS PAGE

AD-A197605

REPORT DOCUMENTATION PAGE

1a. REPORT SECURITY CLASSIFICATION: Unclassified	1b. RESTRICTIVE MARKINGS
2a. SECURITY CLASSIFICATION AUTHORITY: AFOSR	3. DISTRIBUTION/AVAILABILITY OF REPORT: Approved for public release; AFOSR/DTIC distribution unlimited. Approved for public release; distribution unlimited.
2b. DECLASSIFICATION/DOWNGRADING SCHEDULE	
4. PERFORMING ORGANIZATION REPORT NUMBER(S): FR-20424	5. MONITORING ORGANIZATION REPORT NUMBER(S): AFOSR-TR- 88-0771
6a. NAME OF PERFORMING ORGANIZATION: Pratt & Whitney; 6b. OFFICE SYMBOL (If applicable): ME-CT	7a. NAME OF MONITORING ORGANIZATION: Air Force Office of Scientific Research
6c. ADDRESS (City, State and ZIP Code): UTC Pratt & Whitney Group, Government Engine Business, P.O. Box 2691, West Palm Beach, FL 33402	7b. ADDRESS (City, State and ZIP Code): Directorate of Electronic and Mat'l Sciences, Building 410; Bolling AFB DC 20332-6448, Attn: Dr. Alan Rosenstein
8a. NAME OF FUNDING/SPONSORING ORGANIZATION: Air Force Office of Scientific Research; 8b. OFFICE SYMBOL (If applicable): AFOSR/NE	9. PROCUREMENT INSTRUMENT IDENTIFICATION NUMBER: F49620-86-C-0033
8c. ADDRESS (City, State and ZIP Code): Directorate of Electronic and Material Sciences, Building 410; Bolling AFB DC 20332-6448, Attn: Dr. Alan Rosenstein	10. SOURCE OF FUNDING NOS. — PROGRAM ELEMENT NO.: 61102F; PROJECT NO: 2306; TASK NO: A1; WORK UNIT NO:
11. TITLE: Fundamental Understanding of the Intrinsic Ductility in Nickel-Base Ll_2 Type Alloys	
12. PERSONAL AUTHOR(S): C. C. Law, D. M. Shah, J. Lin	
13a. TYPE OF REPORT: Final; 13b. TIME COVERED: FROM 2/15/86 TO 2/14/88; 14. DATE OF REPORT (Yr., Mo., Day): 1988, 6, 30; 15. PAGE COUNT: 82	
16. SUPPLEMENTARY NOTATION	
17. COSATI CODES — FIELD / GROUP / SUB. GR.	18. SUBJECT TERMS (Continue on reverse if necessary and identify by block number): Nickel Aluminide, Single Crystals, Ductility, Strength, Dislocations

19. ABSTRACT (Continue on reverse if necessary and identify by block number)

A basic approach for understanding the ductility behavior of intermetallics through studies of mechanical properties and dislocation characteristics of single crystals was applied to a nickel-base Ll_2 phase compound. Large single crystals of binary and tantalum-modified Ni_3Al alloys with various stoichiometry were produced for tensile testing at 293 to 1144K along four major orientations: <001>, <011>, <111> and <123>. For the binary alloys the tensile ductility generally decreases with temperature for all orientations and reaches a minimum at about 1000K for the nickel-rich (hypostoichiometric) alloy Al240. For a given temperature the ductility decreases in the order <110>, <123>, <001> and <111> in Al240. The ductility of the stoichiometric and hypostoichiometric binary alloys is lower and shows a more complex temperature and orientation dependence than Al240. In contrast to the binary alloys, the ductility of the tantalum-modified ternary alloys shows a rather different

20. DISTRIBUTION/AVAILABILITY OF ABSTRACT: UNCLASSIFIED/UNLIMITED ☒ SAME AS RPT ☐ DTIC USERS ☐	21. ABSTRACT SECURITY CLASSIFICATION: Unclassified
22a. NAME OF RESPONSIBLE INDIVIDUAL: ~~C. C. Law~~ Rosenstein	22b. TELEPHONE NUMBER: (202) 767-4933; 22c. OFFICE SYMBOL: NE

DD FORM 1473, 83 APR EDITION OF 1 JAN 73 IS OBSOLETE.

19. Abstract (Continued)

temperature dependence, either remaining relatively unchanged for orientations deforming primarily by $\{111\}\langle 1\bar{1}0\rangle$ octahedral slip or increasing with temperature for orientations in which $\{001\}\langle 110\rangle$ cube slip dominates. The stoichiometric effect is most pronounced in the ternary alloys. The hypostoichiometric ternary alloy was rather brittle except at the highest temperature.

The orientation and temperature dependence of ductility in all the alloys were shown to be related to the probability and strength of inter-slip interactions of the octahedral and cube slip systems. The probability of interaction was assessed by weighing all the octahedral and cube systems with the magnitudes of the resolved shear stresses and the respective critical resolved shear stresses. Strain hardening was used as an index for the strength of inter-slip interactions. Based on the different types of dislocations observed in these alloys a relationship between the strength of interaction and dislocation features was proposed. A model was developed which satisfactorily mimicked the ductility behavior in a ternary alloy studied. Some alloying directions for improving the ductility in Ni_3Al alloys without compromising the strength are also indicated.

CONTENTS

1.0 INTRODUCTION

The turbine section of a turbofan engine operates under the most extreme conditions. Stresses and temperatures are at high levels and compounded by the steep gradients and complex component geometries. Both turbine blades and disks demand the most advanced mechanical properties to sustain these operating conditions. Nickel superalloys have provided the required characteristics and the success of engines over the past twenty years can be traced in no small measure to the success of these alloys. However, new engines will be required to rotate faster and operate at higher temperatures to achieve the stretch performance goals that have been established. To reach these requirements, radically new approaches to alloy design are needed.

It is generally recognized that development of conventional nickel superalloys has reached a point of diminishing returns and thus new directions must be investigated. One of the approaches to achieve the required property increases is to develop alloys based on intermetallic compounds. The approach is based upon the observation that the ordered structure of compounds often translate into superior high temperature properties. However, engineering application is presently restricted by ductility deficiencies, for most of the high melting temperature intermetallic compounds are rather brittle at ambient temperatures.

The brittleness of intermetallic compounds can be traced to several factors, the lack of grain boundary cohesive strength, microstructure and intrinsic deformation behavior and, in the case of compounds with noncubic crystal lattice, anisotropic thermal properties also. The intrinsic deformation and ductility behavior of intermetallic compounds are the subject of this investigation. There is a general recognition that intrinsic plastic flow behavior is important in governing the ductility and toughness of intermetallics. In particular, the requirements of five independent slip systems for arbitrary deformation at low homologous temperatures is well known. Theoretical studies have also shown the importance of dislocation core structures on dislocation mobility, flow and fracture behavior (References 1, 2 and 3). However, there have been relatively few experimental studies on these deformation features in intermetallics at ambient temperatures due primarily to the fact that most intermetallics of interest are brittle in polycrystalline form at such temperatures. The use of single crystals alleviates such problems and permits the intrinsic flow and fracture behavior of intermetallics to be studied in greater details.

The primary objective of this program is to study the intrinsic flow and fracture behavior of Ni_3Al alloys in single crystal form. There are several rather obvious reasons for this selection. Ni_3Al phase, as the strengthening phase for nickel superalloys, is one of the best known intermetallic compounds. The strength characteristics of Ni_3Al alloys have been subjects of numerous experimental and theoretical studies in the past three decades. Significant advances have been made recently in improving the grain boundary strength of certain Ni_3Al alloys (References 4 and 5), raising the expectation that such an intermetallic may be developed into engineering alloys. However, the ductilizing effect of the boron addition is rather restricted. It fails to ductilize alloys with aluminum content exceeding about 25 atom % (hyperstoichiometric alloys) or alloys rich in solutes, especially those which substitute for Al and provide considerable strengthening such as Ti and Ta. A clue to

the ductility problem in certain polycrystalline Ni_3Al alloys has been provided recently from a Pratt & Whitney study which indicated that, in contrast to the well-known high ductility of the binary Ni_3Al single crystals, certain alloyed Ni_3Al single crystals can be quite brittle depending on specific alloy composition and stoichiometry. This observation suggests that a potentially fruitful approach for improving the ductility and toughness of strong Ni_3Al alloys is through understanding of alloying and stoichiometric effects on intrinsic deformation behavior of such alloys.

1.1 Background and Alloy Selection Logic

Fundamentally, plastic deformation is accomplished by generation and movement of dislocations through a crystal lattice. Thus, the intrinsic ductility of a crystal is governed by the ease with which dislocations are generated and the mobility of these dislocations. It can be shown analytically that both dislocation parameters are influenced by the configurational structure of the dislocations. An ordered lattice increases the number and complexity of potential configurations and various types of structures have been proposed depending on the fault energies (References 6, 7 and 8).

The possible types of dislocation dissociations and their associated planar faults in the $L1_2$ lattice has been summarized recently by Pope and Ezz (Reference 9). Alloying can change the fault energies and favor one type of dislocation configurational structure over the other. For example, addition of Nb, Ta or V to Ni_3Al tends to reduce the antiphase boundary (APB) energy on {001} planes and favor a simple configurational structure consisting of two superlattice dislocations connected by a strip of APB. The change in fault energies in a given lattice can also lead to instability of the lattice toward a derivative structure. These alloying effects on dislocation configurational structure and lattice stability has also been discussed by Pope and Ezz (Reference 9) and by Mishima, et al. (Reference 10) and schematically illustrated in Figure 1. As shown in Figure 1 that addition of Ni, Ta and Sn to nickel $L1_2$ alloys could theoretically lead to three different derivative structures and have the following consequence on the dislocation configurational structure. Addition of Ni in excess of the stoichiometric composition tends to reduce the {111} APB energy and eventually result in A1 structure when added in sufficient quantity. The transition elements Nb, Ta and V tend to reduce the {001} APB energy in the $L1_2$ lattice and transforming it to DO_{22} when added in sufficient amounts. Alloying with Sn tends to reduce the stacking fault (SF) energy of the $L1_2$ lattice and eventually transforming it to the DO_{19} structure.

As results of various changes in fault energies, different types of dissociation of the superlattice dislocations are considered likely to occur in these Ni_3Al alloys. Reducing the {111} APB energy is likely to lead to dissociation by formation of APB and complex stacking faults (CSF) on {111} planes according to the following reaction (Reference 11):

$$[\bar{1}01] = 1/6\ [\bar{1}\bar{1}2] + 1/6\ [\bar{2}11] + 1/6\ [\bar{1}\bar{1}2] + 1/6\ [\bar{2}11] \qquad (1)$$

Increasing the APB energy anisotropy (reducing the {001} APB energy) is likely to result in a simpler dissociation of the type

$$[\bar{1}01] = 1/2\ [\bar{1}01] + 1/2\ [\bar{1}01] \qquad (2)$$

The dissociation which is likely to occur when the SF energy is reduced, is considered to be:

$$[\bar{1}01] = 1/3\,[\bar{2}11] + 1/3\,[11\bar{2}] \qquad (3)$$

which results in superlattice intrinsic stacking faults (SISF) on (111) planes.

There are very few studies of these alloying effects on the type of dislocation dissociations and none attempting to relate the various possible types of dislocation dissociations with the intrinsic deformation and ductility behavior in Ni_3Al alloys.

A primary objective of this program is to study the relationship between the dislocation configurational structure and the deformation and ductility behavior in Ni_3Al alloys. The phase stability concept described above provides a good basis for selection of alloying additions for such a study. To produce a diversity of dislocation configurational structures for study, we selected binary alloys with three levels of Ni content and ternary alloys with additions of Ta and Sn. The concentrations of Ta and Sn were selected to be 5 atom percent and 4 atom percent, respectively which hopefully would be low enough to avoid formation of embrittling secondary intermetallic phases and high enough to produce some effects on dislocation dissociation behavior. The alloys selected which are shown in Table 1, are grouped into three series: the binary alloys, Ta-modified and Sn-modified ternary alloys. The alloys are designated alpha-numerically in which the ternary addition is indicated by the chemical symbols followed by the concentrations of aluminum and the alloying addition, e.g. Sn214 indicates a ternary Ni_3Al alloy consisting of 21 atom percent aluminum, 4 atom percent tin and the balance is nickel.

1.2 Ni_3Al Alloy Intrinsic Ductility Factors and Study Plan

Tensile elongation of the single crystals at fracture was used as a measure of intrinsic ductility on an alloy. Even in a simple uniaxial tension situation the study of intrinsic ductility limiting factors is quite complex. A review of literature suggested that the following factors should be considered (References 9, 12-15):

1. Slip interactions between octahedral systems and octahedral-cube systems.
2. Critical resolved shear stresses for octahedral and cube slip.
3. Dislocation core structure.

The relative importance of these factors depends on test conditions, such as temperature and orientation of the stress axis, and on material parameters such as alloy composition and stoichiometry. To gain insight into the slip system and dislocation interactions we shall analyze the yield strength characteristics, strain hardening and fracture behavior and examine dislocation features using transmission electron microscopy technique. Further, to facilitate the analysis we shall focus on orientations of the following stress axes which would maximize the differences in slip interactions:

<001> No shear stress on the cube planes.
<111> Near maximum shear stress on the cube planes and minimum shear stress on the octahedral planes.
<123> Equal shear stress on cube and octahedral planes.

There is ample theoretical work to show convincingly that dislocation core structure is another important consideration for determining the intrinsic ductility of a crystal (References 1, 2 and 3). In particular, dislocations with planar core structure tend to be more mobile than those whose cores which dissociate on several crystallographically equivalent planes. However, direct observations on the dislocation core structure is difficult, if not impossible, at present. It was proposed that yield strength asymmetry in tensile and compressive tests could be used as an indirect indication of the dislocation core structure (Reference 16). Following the procedures described in Reference 16, <011> orientation of the stress axis, which provides the needed data for determining the tension-compression asymmetry was also included. Finally an attempt was made to integrate some of the experimental observations into a model for predicting ductility behavior of Ni_3Al single crystals.

2.0 EXPERIMENTAL

2.1 Preparation of Single Crystal Specimens

2.1.1 Growth of Single Crystal

Single crystals of alloys given in Table 1 were prepared using a modified Bridgeman crystal growth technique. About 9 kg (20 lb) of each alloy were melted in vacuum by induction heating using high purity elements for the charge. The molten metal was then poured into a preheated ceramic shell mold with a helical crystal starter at the bottom which was in contact with a water-cooled copper chill. After pouring, the mold was slowly withdrawn from the furnace under conditions selected to promote growth of a single crystal. For most runs, the initial withdrawal rate was 76 mm/hour for 100 minutes after which the rate was increased to 102 mm/hour for the remainder of the crystal. Based on previous experiments, this technique typically results in crystals with an <001> growth direction. In some cases several combinations of temperature and growth rate parameters were tried before high quality single crystals could be produced. A schematic diagram of the crystal growing system is given in Figure 2. More details of the directional solidification process for growth of single crystals may be found in Reference [4]. The crystals produced for the current studies are 90 mm in diameter and 180 mm long. Such large crystals are necessary in order to have sufficient material for machining of tensile specimens with stress axes along various major crystal directions. The appearance of the single crystal ingot removed from the shell mold is shown in Figure 3.

2.1.2 Characterization of Large Single Crystal Ingots

The single crystal ingots were centerless ground and macroetched to determine the presence of any secondary grains. Such grains, if present, were marked and the remaining single crystal further characterized using back reflection Laue x-ray diffraction technique. Because of the large dimensions (90 mm diameter, 180 mm long) of the crystals used in our studies, local variations in crystal orientation due to formation of subgrains were often encountered. To obtain an average orientation for the large crystals it was necessary to sample the crystal orientation at different locations on the bottom and top faces of the crystal. Typically five spots were electropolished at each end of the single crystal ingot and x-rayed along the axis of the ingot. Examples of the distribution of crystal orientations determined on several locations from the top and bottom faces of the ingot using Laue diffraction technique, are illustrated in Figures 4, 5 and 6 in which the <001> directions from each location were plotted with reference to three orthogonal axes chosen to be parallel to the axis of the ingot and the dendrite arm directions. The average orientations of the <001> directions are indicated by square symbols in the plots. Figure 4 shows that the <001> growth direction of the Al 240 crystal is several degrees away from the axis of the ingot and that there is relatively little scatter in crystal orientations at various locations in the crystal. The orientation distribution plot for the Ta 195 single crystal, given in Figure 5, shows that the <001> crystal growth direction is nearly parallel to the axis of the ingot but there is relatively large scatter in crystal orientations at various locations, compared with Al 240 (Figure 4). An example which shows both a large deviation of the <001> crystal growth direction from the ingot axis and relatively large scatter in

crystal orientations is shown in Figure 6 for the Ta-10W single crystals. The average orientations of the single crystal ingots defined in this manner were used for machining specimens with axial orientations of <001>, <011>, <111> and <123> as described in the next section.

2.1.3 Machining and Heat Treatment of Specimens

The specific crystallographic data from each ingot determined above were then used to orient the ingot for machining of specimens with stress axes aligned along <001>, <011>, <111> and <123>. The following procedures were used. First, cylindrical slugs about 10 mm diameter were wire electrical discharge machined (EDM) at various angles calculated from the orientation of the ingot to yield cylinders of the selected orientations. Appearance of the crystal section after the slug removal is shown in Figure 7. The specimen slugs were then solution heat treated for 100 hours at 1600°C for the binary and the tantalum-containing ternary alloys and at 1940°C for the two containing alloys. Subsequently, the slugs were hot isostatically pressed (HIP) at the respective solution treatment temperature for 3 hours at 200 MPa. This treatment minimizes the amount of casting porosity in the crystals. The axial orientation of each slug was reconfirmed by x-ray analysis prior to machining of tensile specimens. Plate type tensile specimens with dimensions given in Figure 8 were then wire EDM from the HIP slugs.

2.2 Evaluation of Tensile Properties

Tensile testing was conducted in air at 293, 700, 1033 and 1144K using constant cross-head speed which corresponded to an initial strain rate of 3×10^{-4} per second. If no failure occurred after about 10% strain the cross head speed was increased 10 times till fracture. Tensile elongation was measured from the displacement of two scribed marks on the gage section of the specimen. The tensile yield strength was measured at 0.2% offset and the ultimate tensile strength determined from the maximum load and the initial specimen cross-sectional area. Work hardening rate was measured from the slope of the tensile stress-strain curve at a plastic strain of 5% in which the rates of hardening appeared to reach steady values in tests conducted at 293 and 700K.

2.3 Characterization of Microstructures and Deformation Behavior

The microstructure of each of the alloys was determined using standard optical metallographic techniques. The composition of phases present in selected alloys were studied using a quantitative electron microprobe technique with elemental standards as references.

As tensile testing was conducted in air surface slip line analysis was not possible for most cases due to the oxidized surfaces. The deformation behavior was analyzed using transmission electron microscopy (TEM) techniques. For TEM analysis, 3 mm diameter discs were taken from wafers cut with a diamond saw parallel to the primary octahedral slip plane and both octahedral and cube planes for specimens tested at elevated temperatures. The foils were electropolished using a solution of 6% perchloric acid in equal parts of methanol, ethanol and butanol in a Fischione twin jet electropolisher operated at 30V, 7 mA/mm, and 258K. The dislocation characters and nature of stacking faults was studied in various diffraction contrast conditons. The a/2<110>

type dislocations were identified using g·b = 0 criterion, and the criterion outlined by Kear et. al (Reference 18) when a/3<211> dislocations will be invisible if g·b = 0, ±1/3, -2/3 or +4/3 and visible if g·b = +2/3, -4/3, ±1 or ±2. The intrinsic/extrinsic nature of stacking faults was determined by observing changes in fringe contrast at the top and bottom of the foil followed the procedures of Howie and Hashimoto et. al (Reference 19).

3.0 RESULTS

The preparation of the large single crystals 90 mm in diameter and 180 mm long proved to be a major challenge. It was found that crystals of some alloys could be grown relatively easily while others required several runs, each with a different combination of temperature and growth rate parameters, before high quality single crystals could be produced. Unfortunately, growth of large single crystals of Al 250 and Sn 234 was unsuccessful despite several trials for each of these alloys. Smaller crystals (25 mm diameter bars) of Al 250 were produced which necessarily limited the scope of evaluation for this particular alloy. Many Sn 234 single crystals were obtained under the wide range of growth conditions. The analyzed compositions of the single crystal ingots are given in Table 2 and show only minor deviations from the aim

3.1 Microstructure

The microstructures of all the binary alloy single crystals in the as-cast condition consist of NiAl and Ni_3Al phases (Figure 9). The amount of the NiAl phase increases with increasing Al content and about 10 volume percent was observed in Al 270 in which the NiAl phase formed as dendrites. The microstructures of the Al 250 and Al 270 remained essentially unchanged while Al 240 was almost completely homogenized after the heat treatment at 1477K for 100 hours. The phase compositions of alloys Al 250 and Al 270 were determined using electron microprobe techniques and the results are given in Table 1 which show that the Ni_3Al is slightly hypostoichiometric and hyperstoichiometric in alloys Al 250 and Al 270, respectively

The microstructures of the tin-containing Ni_3Al alloys appear rather similar. The differences are primarily in the amount and distribution of the phases. Therefore, microstructure and electron microprobe results are presented for Sn 214 only, other alloys showed similar results. Figure 10 shows scanning electron micrographs of the microstructure of Sn 214 single crystal in the as-cast condition. The presence of three different phases, labelled A, B and C in Figure 10b, is apparent. Heat treating the alloy for 50 hours at 1339K produced no important changes in the microstructure (Figure 11) although the phase boundaries became more distinct. As shown in Table 4, some changes in phase composition took place during heat treatment. Table 4 also shows that Phase A, the major constituent, is the ternary L1$_2$ phase Ni_3Al, phase B is probably a DO_{19} phase Ni_3Al substituting at the Sn sublattice and Phase C is probably a B8 type compound Ni_3Sn_2, again with some substitution of Al on the Sn sublattice. As will be shown later, these secondary intermetallic phases are rather brittle and resulted in premature failures of all the Sn-modified single crystal specimens.

The microstructures of the tantalum-containing Ni_3Al alloys consist of Ni_3Al and NiAl phases. As expected, the amount of the NiAl phase increases with the aluminum content and reaches about 8 volume percent in alloy Ta 227 which contains the highest Al content. Both the microstructure and phase composition in the tantalum-containing alloys were found to be rather stable; only minor changes resulted from a heat treatment for 100 hours at 1477K (Figure 12). The compositions of the phases in alloy Ta 225 are shown in Table 5 which shows a much larger solubility for Ta in Ni_3Al, than in the NiAl phase. Further, if one assumes that all the Ta atoms occupy only the Al

sublattice sites, then the $L1_2$ phase in Ta 225 is hyperstoichiometric as intended.

3.2 Strength of Ni_3Al Alloys

3.2.1 Yield Behavior

A comparative study of yield strengths in the binary and ternary alloys is considered crucial to a basic understanding of the ductility of this class of materials. Tensile testing was conducted in the four major orientations <001>,<011>,<111> and <123> between room temperature and 1144K at a nominal strain rate of $3x10^{-4}$ per second. To provide a further characterization of plastic anisotropy compression tests were also conducted in the <001> and <011> orientations at approximately the same strain rate condition for two off-stoichiometric variants of both the binary and tantalum-modified alloys. These orientations were chosen since they are known to show a maximum flip-flop in tensile and compressive yield strengths (Reference 9).

It was noted that the ductility of the tin-modified alloys An 204 and Sn 214 was consistently low, generaqlly below 5% regardless of the orientation of the stress axis and that the tensile yield strengths were found to be considerably lower than those obtained in compression. Sectioning of tensile tested specimens revealed extensive cracking of the secondary phases, as shown in Figure 13, which no doubt resulted in the low apparent tensile yield strengths and premature tensile failures observed. Therefore, the tensile data obtained for the tin-containing alloys will not be discussed any further. The tensile yield strength and the ultimate tensile strength are plotted against temperature for all the four major orientations for the alloys Al 240, Al 250 and Al 270 in Figure 14 and for alloys Ta 195, Ta 205 and Ta 225 in Figure 15. The results are also listed in Tables 7 to 12 for each alloy in with angular coordinates describing actual axial orientation for each specimen. It can be verified that in almost all cases the actual orientation is within 10° of the designated major orientation. Thus for most of the qualitative discussion the designated orientation is sufficiently accurate. However, for quantitative evaluation of resolved shear stresses the actual calculated values were used as listed in the tables.

Note that in all six alloys there is evidence of an increase in yield strength with temperature at least for the <001> orientation. For the nickel-rich binary alloy (Al 240) the anomalous behavior is strongly displayed by all orientations and the yield strengths reach a maximum at about 1000K. With increasing aluminum content, the yield strength peak temperature shifts to 700K. Nonetheless, the absolute level of strength and the nature of the orientation dependence of the yield strength are not altered significantly. In contrast, for the ternary alloys with increasing aluminum content, the peak temperature is lowered to a lesser extent but the absolute level of strength and the orientation dependence of strength are strongly affected. Note for example that for the nickel-rich Ta 195 the <111> orientation is stronger than <001> orientation below 800K but for the stoichiometric alloy Ta 205 <001> orientation is significantly stronger than <111> orientation at all temperatures above room temperature. In other words while the strength cross-over between <001> and <111> orientations occur at around 800K in the case of Ta 195, for Ta 205 and Ta 225 it occurs near room temperature. The temperature dependence of ultimate tensile strength parallels the observations for yield

strength, albeit at a higher strength level showing lesser anomalous rise in strength.

To understand the yield strength observations in a fundamental sense, it is essential to analyze the results in terms of resolved shear stresses on the operating slip systems for the materials. This is a trivial exercise for materials deforming by one family of slip systems with Schmid's law being strictly obeyed. Such would be a case for disordered solid solution alloys with face centered cubic (fcc) structure where deformation can be assumed to occur on octahedral slip systems with little deviation from Schmid's law. Conformance to Schmid's law allows determination of a unique value of critical resolved shear stress (CRSS) for the operating slip system, independent of the orientation of the stress axis. However, for the class of $L1_2$ ordered compounds under consideration two factors complicate such an analysis. First, even without considering other complicating factors (see later discussion) the deformation behavior must be described in terms of two possible slip systems. These are $\{111\}\langle 1\bar{1}0\rangle$ octahedral type slip systems and $\{100\}\langle 110\rangle$ cube type slip systems. Secondly, it is well established that Schmid's law is not strictly obeyed. That is the CRSS is not an invariant with orientation of the stress axis. The CRSS for octahedral slip is perturbed by the dislocation core transformation due to the constricting shear component of the stress tenser in <112> directions (Reference 16). This deviation is best assessed by the tension/compression asymmetry as presented later in this section. Nevertheless for the purpose of comprehending the preceding complex observations of yield strength behavior, it is useful to phenomenologically assume that the two slip systems operate independently without mutual perturbation and that the Schmid's law is approximately valid.

With those simplifying assumption the temperature dependence of the CRSS for octahedral slip can be easily deduced using the actual resolved shear stress (RSS) values for the <001> orientation. These values are calculated for each alloy and listed in Tables 7 to 12. The choice of <001> orientation is appropriate since the resolved shear stress for cube slip in the vicinity <001> is insignificant. The determination of CRSS for cube slip, however, needs some extrapolation. At temperatures where the yield strength of <111> orientation is comparable or lower than the yield strength of the <001> orientation, the CRSS for cube slip can be calculated using the yield strength values for the <111> orientation. This is valid since it can be shown that if octahedral slip were the only operative slip system, then based on the ratio of Schmid factors the yield strength of <111> orientation should be exactly 1.5 times the yield strength of <001> orientation. Thus for comparable yield strength values for the <001> and <111> orientations, independent operation of cube slip can be safely assumed. At temperatures where the yield strength of <111> orientation is higher than that of <001> orientation, it is not possible to determine the CRSS of cube slip without possibly studying pure shear deformation. In this case the CRSS for cube slip is assumed to increase with decreasing temperature and the low temperature values determined by extrapolation. In this manner CRSS as a function of temperature for both cube and octahedral slip has been deduced for four alloys as presented in Figure 16. The extent of error shown by shaded band for the CRSS plot of octahedral slip is derived from a tension compression asymmetry experiments as discussed later.

A comparison of these plots of CRSS versus temperature in Figure 16 clearly shows the trend in the interrelation between the CRSS of the two slip systems for the four alloys representing the extremes in the binary and ternary alloys. For the nickel rich binary alloy Al 240 the cross-over between the CRSS of cube and octahedral slip occurs at the highest temperature of around 925K among the alloys evaluated. With increasing aluminum content for the alloy Al 270 the cross-over temperature is decreased though not sharply defined. For the ternary nickel rich alloy Ta 195 the cube slip becomes a competing slip mode at even lower temperature. Finally the aluminum rich ternary alloy the two slip systems become equal in strength at as low as 600K. These observations are consistent with our observations of dislocation structure in these alloys. No clear evidence of cube slip has been obtained for the binary nickel-rich alloy Al 240 where cube slip is expected to be activated at higher temperature only. In contrast for ternary alloys evidence or cube slip is readily obtained consistent with the low CRSS for cube slip at lower temperature. It is also interesting to note that while the CRSS for octahedral slip is significantly enhanced at lower temperatures with ternary additions, the CRSS for cube slip is not altered to a great extent. The implication of these findings on ductility will be discussed in Section 4.0.

3.2.2 Tension/Compression Asymmetry of Yield Strength

In the preceding section it was noted that the assumption of strict validity of Schmid's law is not correct. To assess the deviation from Schmid's law, which is attributed to dislocation core constriction effect, compression tests were carried out at room temperature and 700K for the alloys Al 240, Al 270, Ta 195 and Ta 225 in both <001> and <011> orientations. The results are presented in Table 13. The room temperature data for all four alloys are also compared using in Figure 17. The data for 700K are similar in nature except for the Al 240 alloy. If Schmid's law were strictly valid one would expect both <001> and <011> orientations to have equal yield strength both in tension and compression since the Schmid factors in both orientations are identical for octahedral slip system. Clearly such is not the case for the ternary alloys is apparent from Figure 17. The deviation is of the order of 100 and 200 MPa for the Ta 195 and Ta 225 alloys respectively. This is consistent with the observed tension/compression asymmetry for tantalum and niobium modified ternary alloys as published in the literature (References 9 and 16), in both cases here the <001> orientation is observed to be stronger than <011> orientation in tension and vise versa in compression. This behavior is quite well explained in terms of a constriction stress parameter which either leads to constriction or extension of superdislocation core structure thereby aiding or abating the cube-cross slip process and effectively enhancing or reducing the CRSS for octahedral slip respectively. The critical aspect of the mechanism is that the behavior is reversed in going from tension to compression for the same orientation. Qualitatively a greater magnitude of asymmetry represents a wider spread of core structure. For dislocations with a truly singular core structure, it is difficult to envision effect of any other component of stress tensor, other than the resolved shear stress on the glide plane, playing significant role in determining the motion of dislocation. Dependence of deformation behavior on more than one shear component of the stress tensor is essentially observed as deviation from Schmid's law.

For the binary alloys, owing to the lower absolute magnitude of the stress it is difficult to convincingly conclude any significant deviation from Schmid's law. Considering a variation in crystallographic orientation and the fact that the tension and compression tests were not carried out on the same specimens, the deviation in strength does not seem statistically meaningful. Nevertheless to be consistent we have attempted to estimate the extent of error involved in deducing the CRSS for octahedral slip system as plotted in Figure 16 for all alloys. This is calculated as a difference between the maximum and the minimum values of the yield strengths for the <001> and <011> orientations at room temperature for all alloys. A shaded band equivalent to this difference is shown in Figure 16 for the CRSS curves for octahedral slip and is allowed to shrink with increasing temperature to reflect the fact that one expects the effect to vanish at higher temperatures. Even with this crude quantitative estimate, it is clear that the deviation from Schmid's law increases with increasing aluminum content and ternary addition. Thus the decrease in the cross-over temperature of the CRSS of cube and octahedral slip systems parallels an increase in tension compression asymmetry or deviation from Schmid's law in going from a nickel rich binary alloy Al 240 to aluminum rich ternary alloy Ta 225. Without further theoretical development it is difficult to understand the factors affecting the dislocation core structure and the relative values of CRSS for the two slip systems.

Note that in all six alloys there is evidence of anomalous increase in yield strength with temperature at least for the <001> orientation. For the nickel-rich binary alloy (Al 240) the anomalous behavior is strongly displayed by all orientations and the yield strengths reach a maximum at about 1000K. With increasing aluminum content, the yield strength peak temperature shifts to 700K.

3.3 Strain Hardening

Generally, for a given test condition the rate of strain hardening in an alloy changes depending on the level of strain/dislocation structure. For single crystals, stages of strain hardening have been observed which were shown to be associated with different dislocation mobilities (Reference 20). Figures 18 and 19 show examples of the tensile stress and strain behavior for some of the alloys studied - Al 240 and Ta 195 at 293K, 700K, 1033K and 1144K. The strain hardening behavior is seen to be dependent on the orientation of the stress axis, temperature, alloy composition and strain level. For a given alloy and specific stress axis orientation, the work hardening rate is relatively constant with strain at the two lower temperatures. However, at higher temperatures, softening, following initial strain hardening, can be observed in both alloys. This phenomenon is more pronounced in the binary alloys, indicating operation of thermally activated recovery mechanisms. We shall restrict our ductility study primarily to lower temperatures where recovery is not an important complicating factor. Strain hardening measurements were made, whenever possible, at about 5% strain when the rate of hardening approaches a steady state value for most alloys. However, as will be shown in Section 3.4 a number of specimens failed at less than 5% strain and therefore, observations of their strain hardening behavior as a function of stoichiometry and alloying addition are rather limited. Figures 20 and 21 show the strain hardening data for the binary alloys and the tantalum-modified ternary alloys at 293K and 700K. Several interesting trends can be observed from these figures. In the binary alloys, the work hardening increases with increasing

temperature and aluminum content. For a given temperature and stoichiometry the working hardening also changes with the orientation of the stress axis, and in the binary alloys work hardening increases in the following order: <110>, <123>, <001> and <111>. In this case a clear correlation of strain hardening and ductility can be made, ductility is inversely related to strain hardening. Ductility results will be presented in Section 3.4.

The strain hardening behavior of the tantalum-modified alloys differs from that of the binary alloys in several important ways. For a given orientation and at room temperature the magnitude of strain hardening is generally higher in the ternary alloys than the binary alloys of corresponding stoichiometry. As will be shown in Section 4.3, differences in work hardening between the binary and ternary alloys are basically related to the type of dislocations present. At 700K, the strain hardening in the ternary alloys is reduced rather than increased as in the binary alloy. As will be shown in Section 3.5, the drop in strain hardening in the ternary alloy at higher temperature is related to the activation of the {001}<110> slip mode. An inverse relation between strain hardening and ductility can also be observed in the ternary alloys.

3.4 Tensile Ductility

The general effects of alloy composition and test temperature on the tensile ductility of boron-doped polycrystalline nickel base $L1_2$ alloys are now well known. In particular, ductility decreases with increasing aluminum content and/or additions of strengthening solutes and with increasing temperature. The drop in ductility at low temperatures is usually attributed to a compositional effect on the grain boundary segregation behavior of boron (Reference 21). The decrease in ductility with increasing temperature has been attributed to environmental effects (Reference 22) and deformation on {001}<110> slip systems (Reference 23). One of the objectives of this program are to determine the relative importance of these ductility limiting factors and provide insights into the intrinsic ductility behavior of the nickel-base $L1_2$ alloys.

Tensile ductility of single crystals of binary alloys with aluminum levels of 23.5, 25.0 and 26.5 atom percent (alloys Al-240, Al-250 and Al-270) and their tantalum-modified counterparts Ta-195, Ta-205 and Ta-225 are shown as a function of stress axis orientation and temperature in Figure 22. First examining the ductility behavior of Al 240, one sees that the ductility in this alloy is strongly influenced by the orientation of the stress axis. Below the yield stress peak temperature, at about 1033K, the ductility decreases in the order <011>, <123>, <001> and <111> and for a given stress axis orientation, the ductility decreases with increasing temperature. Both of these ductility trends can be correlated with the work hardening behavior described previously in Section 3.3. Higher ductility is associated with lower work hardening. The relationship between stress orientation, ductility and work hardening is treated analytically in Section 4.0

Several interesting alloy compositional effects are obvious from Figure 1. Generally the ductility decreases with increasing aluminum content at temperatures below the yield strength peak. The hypostoichiometric alloys Al 240 and Ta 195 are considerably more ductile than the hyperstoichiometric alloys Al 270 and Ta 225 respectively. The stoichiometric effect on ductility

is especially pronounced in the case of the tantalum-modified alloys. This observation indicates clearly that the poor ductility observed in the boron-doped hyperstoichiometric alloys in polycrystalline form is basically related to the intrinsically poor ductility in such alloys rather than a compositional effect on boron segregation to grain boundaries. As will be shown, the reduction of ductility with increasing aluminum content is accompanied by changes in dislocation structure and fracture behavior.

Addition of a strengthening solute such as tantalum alters the intrinsic ductility in two important ways relative to the binary alloys. Ductility levels of the ternary alloys are lower, except at temperatures slightly below the yield strength peak. At such temperatures the tensile ductility of the ternary alloy is enhanced, rather than reduced as in the case of the binary alloys. The ductility enhancement in the ternary alloys is most pronounced in the <111> and <123> crystals. As will be shown later, the ductility improvements in these crystals resulted from slip on {001}<110> systems which become more favorable than the {111}<110> systems at temperatures near the yield strength peak. Although the operation of the {001}<110> systems can lead to high ductility in a solute strengthened alloy in single crystal form, it tends to reduce the ductility of the alloy in polycrystalline form due to strain incompatibility at grain boundaries. Thus one would expect the ductility of polycrystalline Ta 195 to be lower than Al 240 at room temperature and the difference would be larger at temperatures slightly below the yield strength peak. This has indeed been observed (Reference 24).

3.5 Dislocation Characteristics and Deformation Behavior

3.5.1 Binary Ni_3Al Alloys

We shall start with the stoichiometric Ni_3Al alloy, a baseline for observations on off-stoichiometric effects. Recently, Baker and Schulson studied in detail the dislocations and stacking faults in the stoichiometric alloy as a function of deformation temperature in the range 77 to 1032K (References 25 and 26). Partly out of necessity because of our unsuccessful attempts to grow large single crystals of this alloy, we shall use primarily Baker and Schulson's results as a reference. Baker and Schulson observed two types of dislocations in the stoichiometric Ni_3Al alloy: anti-phase boundary (APB) coupled screw dislocations with a Burgers vector of a/2<110> and superlattice intrinsic stacking fault (SISF) - coupled dislocations with a Burgers vector of a/3<211>. At low temperature (77 to 673K) both types of dislocations were found to be present and at high temperatures (873 to 1023K) most dislocations were observed to be the APB pairs. In addition, a transition from octahedral {111} slip to cube {001} slip was found to occur near the yield strength peak temperature. Figure 23 shows the appearance of dislocations in Al 250 produced by straining along <111> at 1144K. At least two sets of dislocations can be observed. Diffraction contrast analysis indicated that the dislocations were APB-coupled screws with a/2[101] and a/2[101] Burgers vectors and lie on cube (010) planes. These observations are entirely consistent with Baker and Schulson's results.

Tensile straining of the hypostoichiometric Al 240 at 293K resulted in both stacking faults and dislocations which both lie on {111} planes (Figure 24). The stacking faults were determined to be of the SISF type. However, the exact character of the dislocations has not yet been determined. Electron

diffraction contrast results indicated that these dislocations were definitely not the APB-coupled screws. The presence of SISF suggests perhaps SISF-coupled dislocations as observed by Baker and Schulson in the stoichiometric alloy. However, diffraction contrast experiments were unable to confirm the a/3<112> type dislocations as the bounding partials. Perhaps a more complex dislocation dissociation scheme is operative in Al 240 which involves the formation of APB and complex stacking fault (CSF) and a/6<112> partial dislocations as described by equation (1) (Section 1.0) which was proposed by Marcinkowski et al. (Reference 11). On the other hand, a different type of dislocation was produced in Al240 by straining at 1033K (Figure 25). In this case the dislocations were unambiguously identified as the APB-coupled screws having an a/2<110> Burgers vector, similar to those observed in the stoichiometric alloy. However, unlike the stoichiometric alloy, cube slip was not observed in Al 240 up to the highest test temperature (1144K) even for the most favorable stress condition (straining along <111>). Thus, reducing the aluminum content promotes SISF type dislocations at low temperatures and suppresses cube slip at high temperatures.

Turning now to the hyperstoichiometric Al 270, the dislocations observed here are APB-coupled screws with a/2<110> Burgers vectors. The type of dislocations remain unchanged for deformation in the temperature range studied of 293 to 1144K. Further, no SISF were found in this alloy. Although the dislocations produced by high temperature deformation are similar for all the binary alloys, important differences in the spacing of the superlattice partials bounding the APB can be observed as shown in Figure 26. The spacing of the partials which were imaged using a weak beam dark field technique were measured to be 5 nm and 3.5 nm and the calculated APB energies are 163 and 233 mJ/m^2 for Al 240 and Al 270, respectively, indicating an increase in APB energy with increasing aluminum content. As in the stoichiometric alloy, cube slip was also observed in Al 270 after high temperature deformation. Figure 27 shows the dislocation activity on (001) plane resulting from about 4% tensile strain along <123> at 1033K. Thus increasing the aluminum content suppresses the formation of SISF and increases the APB energy.

3.5.2 Tantalum-Modified Ternary Ni_3Al Alloys

Relative to the binary alloys, three important differences were observed. Throughout the entire temperature range studied of 293 to 1144K, the dislocations in Ta 195, Ta 205 and Ta 225 were found to be similar and are the APB-coupled screws with a/2<110> Burgers vectors. No stacking faults were observed in specimens deformed at 293K even for Ta195 which has the lowest aluminum content (Figure 27). Secondly, the spacing of the dislocation pairs in the ternary alloys must be considerably less than the smallest spacing of 3.5 nm determined in the binary alloy Al 270, as it was not possible to resolve the dislocation pairs even in Ta 195 which is expected to have the largest spacing in this alloy series. Thirdly, cube slip occurs more readily in the Ta- modified alloys than in the stoichiometrically equivalent binary alloys. Figure 28 shows profusion of slip on (100) planes in Ta 195 due to straining at 1033K; no cube slip in Al240 was observed even at 1144K. Further, evidence for cube slip at even lower temperatures in this alloy can be observed in the ductility versus temperature curve shown in Figure 22. The rapid rise in ductility with increasing temperature starting at 600K in the specimens strained along <111> and <123> axes is a strong indication of cube slip activity.

In summary, the effects of tantalum additions on the dislocation and deformation behavior in Ni_3Al appear to be similar to increasing the aluminum content in binary Ni_3Al. Either alloying change suppresses the formation of SISF, increases APB energy and promotes cube slip. On a per atom basis, the tantalum effects are more potent.

3.6 Fracture Behavior

In the final analysis, it is the fracture which limits the ductility of an alloy. Thus, basic understanding of the fracture mechanisms and fracture criteria of single crystals would provide additional insights into the intrinsic ductility behavior. In the present program, fracture in the binary Ni_3Al and tantalum-modified single crystals were studied as a function of alloy stoichiometry, stress axis and temperature. Fracture surfaces were characterized in terms of the general appearance and orientations of the shear facets which were determined primarily from geometric measurements. Limited x-ray diffraction measurements were also used to confirm results derived from geometrical measurements. In fractures which consist of small facets the indexing of the facets was experimentally more difficult and results are less certain. The appearances of fracture in the binary alloys Al 240 and Al 270 at 293 and 700K are shown in Figures 29 and 30, respectively and the orientations of the shear facets summarized in Table 6. It can be seen from these results that the fracture behavior in Ni_3Al alloys is quite complex. It varies significantly with alloy composition, temperature and stress axis. For a given temperature and alloy composition, for example Al 240 at 293K, fracture on {100}, {110} and {111} was observed depending on the specific orientation of the stress axis. The observations in binary alloys are in contrast to those by Aoki and Izumi on $Ni_3(Al, Ti)$ and Ni_3Ge in which they observed that fractures in these two compounds occurred by cleavage on {001} facets only (References 13 and 14). Further, Aoki and Izumi showed that the fractures in $Ni_3(Al, Ti)$ and Ni_3Ge occurred when the normal stress on the {001} planes reached a critical value, i.e. the normal stress fracture criterion applied. Because the fracture in binary Ni_3Al crystals occurs on different fracture planes depending on the stress axis orientation, obviously the fracture criterion is more complex. The fracture behavior of the tantalum-modified alloys is different from the binary alloys but equally complex. At present, we are unable to determine quantitatively an appropriate fracture criterion for either the binary or the tantalum-modified alloys. However, the following approach is suggested for future development of fracture criteria in Ni_3Al alloys.

The approach is based on two important observations. There was no necking in fractures below the peak yield stress temperature in both alloy systems, indicating that, macroscopically, fractures at these temperatures occur in a brittle manner. Secondly, surface cracks were often observed prior to fracture. These observations suggest a critical stage in the fracture of these alloys is the formation of surface cracks of critical size. Thus, an appropriate fracture criterion will have to take into consideration the mechanisms of surface crack formation and propagation. Since surface steps could provide stress concentrations as large as cracks (Reference 27), they also could be considered as a candidate for fracture initiation. Of interest for intrinsic ductility are the surface steps produced by slip. For a given surface step radius and angle, the stress concentration increases with the step height (Reference 27). It could be hypothesized that a surface crack

would form when the stress concentration/step height reaches a critical value. Mechanistically this means that a crack would form after a critical amount of shear on a slip system. We shall use this concept in modeling the ductility behavior in the Ni_3Al alloys in Section 4.2.

4.0 DISCUSSION

An important barrier to development of intermetallic compounds for high temperature applications is the brittleness observed at various temperatures. One of the objectives of this program is to gain insight into the brittleness problem through a basic understanding of the relationship of dislocation behavior and tensile ductility of the compound in single crystal form (intrinsic ductility). The compound selected, the $L1_2$ ordered Ni_3Al, exhibits many complex dislocation characteristics and serves as a good prototype for other intermetallics. Current theoretical understanding of alloying effect on $L1_2$ phase stability and dislocation structural configurations indicate that macroalloying technique could be used to produce a variety of dislocation behavior in the Ni_3Al phase. The selected alloying changes were modification of nickel content (stoichiometry), addition of tantalum and tin. The expected dislocation structural configuration, summarized schematically in Figure 1, were CS/APB coupled dislocations in nickel-rich (hypostoichiometric) binary alloys, APB-coupled dislocations in tantalum-modified alloys and SISF-coupled dislocations in tin-modified alloys. Further, the tantalum addition tends to result in nonplanar dislocation core structure, adding yet another variation in dislocation behavior. Nine alloys with compositions given in Table 1 were selected. Since the ductility in Ni_3Al single crystal is known to be anisotropic and temperature dependent tensile testing of the single crystal specimens was conducted on stress axes <001>, <011>, <111> and <123> and at 293, 700, 1033 and 1144K. The stress axes were selected to study the interaction of octahedral and cube slip and the tension-compression yield strength asymmetry which is an indication of dislocation core structure. To fabricate tensile specimens of these orientations and with dimensions adequate for realistic tensile tests, large single crystals 90 mm diameter and 180 mm long were grown. No previous single crystal study program of this magnitude is known to the authors. To produce such large crystals of the selected nine alloys and the necessary background of the solidification behavior in most cases, proved to be a major task. We were successful in producing good quality large crystals of the selected alloys except Al 250 and Sn 234. Single crystals of Al 250 were produced as 25 mm diameter ingots but the growth of Sn 234 single crystal was unsuccessful using a variety of growth conditions. Thus only eight alloys were tested. Unfortunately results from only six alloys were useful all the tin-containing specimens failed prematurely by cracking initiated in the secondary intermetallic phases which formed in the alloys during solidification.

As noted above the focus of this study was the attempt to explain tensile ductility elucidated by dislocations and tension-compression asymmetry techniques. In addition strength levels, strain hardening and fracture behavior of the crystals were also studied. Important results are summarized and discussed below.

4.1 Effect of Temperature and Orientation on Ductility

Results summarized in Figure 22 show that the ductility behavior is rather complex. Both orientation and temperature have major effects on ductility and the effects vary significantly between alloys. For the binary alloys ductility generally decreases with increasing temperature for all orientations and reaches a minimum at about 1000K for Al 240. The ductility minimums for the Al 250 and Al 270 are in the temperature range 700K to 1000K

depending on specific orientations. For a given temperature in Al 240 the ductility decreases in the order [illegible] except near the ductility minimum where the <111> orientation appears to be more ductile. The orientation-ductility relationships are more complex in the other two binary alloys.

In contrast to the binary alloys, the ductility of the tantalum-modified ternary alloys show a different temperature dependence, either remaining relatively unchanged or increasing with temperature depending on the specific orientation. Most remarkable is the rather rapid increase in ductility with temperature in the <111> and <123> orientations especially in Ta-9%

To fully explain the complex ductility behavior requires a detailed knowledge of the operative slip systems as a function of orientation and temperature, crack initiation mechanism and fracture criterion in these alloys. However the main features of the ductility pattern can be accounted for if we concentrate on the plastic flow features of the process. The following analysis is probably more applicable to low temperatures, the known influence of environment at higher temperatures could complicate the picture although the extent of the effect in single crystals is not well documented. The CRSS data shown in Figure 16 indicates the relative ease of flow on the two major competitive systems, octahedral and cube slip. In principle the ductility of a crystal can be related to the number and mobility of dislocations. The interaction of dislocations on intersecting slip planes can lead to immobilization or locking of dislocations by the Cottrel-Lomer mechanism, for example. In the $L1_2$ lattice other important factors include the octahedral: cube cross slip process and the tendency to nonplanar core structures for certain alloys. We have not attempted to analyse the details of these processes directly but consider that the number of dynamic slip system interactions will be a measure of the frequency of immobilization events and that work hardening rate will be an index of the strength of the interactions. Thus by using the CRSS information, shown in Figure 16 and the work hardening rates summarized in Figures 21 and 22 ductility trends can be explained. For example in alloy Al 240 only octahedral slip systems can be activated because of the high CRSS on the cube system. As predicted the <123> and <110> orientations which have larger shear stress on the octahedral systems and/or smaller number of competing slip systems show higher ductility than <111> and <001> orientations. As temperature increases, the cube slip systems become increasingly favored thus increasing the slip interactions which may account in part for the general drop in ductility. The proximity of the temperatures of ductility minimum and the cross-over of the CRSS for octahedral and cube slip may be significant. The ductility trends in Al 270 can be explained similarly. Note that in Al 270, the relative differences in CRSS between the octahedral and cube systems are considerably smaller and the equi-CRSS temperature is also lower. This could partly explain the generally lower ductility level and lower temperature for minimum ductility in this alloy compared with Al 240.

The next section develops a quantitative model for these processes and can account for the ductility behavior within alloys. However, it cannot account for the large effect of alloy composition on the absolute values of ductility, an issue that is treated in Section 4.3.

4.2 Modeling of Orientation Dependence of Ductility

Experimental determination of orientation dependence of ductility was carried out with the objective of gaining an insight into the intrinsic ductility. The concept was to use the crystallographic orientation of a simple tensile state of stress as a variable to probe the behavior of two slip systems and the interaction between them. As a first step towards achieving this objective an attempt has been made to rationalize the orientation dependence of ductility by evolving a mathematical model. The model is aimed at providing a quantitative expression for two qualitative concepts which are well recognized. The first concept or requirement is that in a single crystal body the total strain must be resolved as shear strains distributed among various slip systems somehow in proportion to the resolved shear stresses as well as satisfying compatibility conditions. Thus a symmetric orientation is expected to deform by multiple slip systems and an unsymmetrical orientation by largely a single slip system with extensive rotation. The second concept is that the larger the number of operating slip systems, the larger may be the interaction and work hardening. Thus for a symmetric orientation, greater interactions from other slip systems are expected with an increase in work hardening and decrease in ductility. While for an unsymmetrical orientation deforming by single slip, a lesser amount of work hardening is expected with higher ductility.

However, if there were no interactions between the slip systems the concept of proper shear strain distribution would indicate the multiple slip, symmetric orientation to have the largest tensile ductility and the single slip orientation to have the least. This is on the assumption that fracture will occur at an equal shear strain on the operating slip system irrespective of the orientation of the tensile axis. Clearly the concept of strain distribution and the mutual interactions between the slip systems act in opposition. Furthermore, except for the most symmetric orientation at the corners and boundaries of a standard stereographic triangle there are no orientations which can be classified either as single or multiple slip. One of the objectives of the model is to mathematically provide a weighing of various slip systems based on the relative values of the resolved shear stresses, so that all orientations can be treated in a continuous manner and the opposing effects of strain distribution and mutual interactions on ductility can be assessed on a more quantitative basis.

For a large deformation, rigorously it is essential to consider the rotation of the stress axis. However, it can be shown that ignoring the rotation , even at a total strain of 50%, introduces no more than 4% error than the tensile strain calculated using the following simple relationship

$$\epsilon_{ii} = (a_{ij} \cdot a_{ik}) \ \gamma_{jk} \qquad (1)$$

where ϵ_{ii} is the tensile strain
γ_{jk} is the shear strain on the operative slip system (jk) and
a_{ij} and a_{ik} are cosines of angles between the stress axis and the slip plane (j) and slip direction (k) respectively.

In a more familiar term

$(a_{ij}.a_{ik})$ is the Schmid factor for the slip system.

Accepting Equation (1) as approximately valid, the total tensile strain in an $L1_2$ compound deforming by both octahedral and cube slip systems must be expressed as follows:

$$\epsilon_{ii} = \sum^{\text{Oct.}} |\, a_{ij}.a_{ik}|_o \cdot \gamma_{jko} + \sum^{\text{Cube}} |\, a_{ij}.a_{ik}|_c \cdot \gamma_{jkc} \qquad (2)$$

The additional subscripts (o) and (c) in all equations refer to octahedral and cube slip systems, respectively.

Now in order to achieve an approximately correct strain distribution we shall ignore any compatibility constraints by assuming a freely deforming volume of material. In addition, we will assume that for each family of slip systems a characteristic linear relationship exists between the shear strain and shear stress which is independent of strain rate. In making this assumption we are allowing deformation to take place well below the CRSS for the particular slip system. If this is not done, it is difficult to account for interactions from other than primary slip systems without invoking a complex integration process.

Thus we assume that

$$\gamma_{jko} = B_o\, \tau_{jko} = B_o\, |\, a_{ij}.a_{ik}|_o \cdot \sigma_{ii} \qquad (3)$$

and

$$\gamma_{jkc} = B_c\, \tau_{jkc} = B_c\, |\, a_{ij}.a_{ik}|_c \cdot \sigma_{ii} \qquad (4)$$

where σ_{ii} is the applied tensile stress.

Substituting Equations (3) and (4) in Equation (2) yields:

$$\epsilon_{ii} = \left[B_o \sum^{\text{Oct.}} |\, a_{ij}.a_{ik}|_o^{\,2} + B_c \sum^{\text{Cube}} |\, a_{ij}.a_{ik}|_c^{\,2} \right] \sigma_{ii} \qquad (5)$$

Now we can relate the shear strain on the primary slip system and the total tensile strain again using the Equation (2) as follows.

$$\epsilon_{ii} = \frac{B_o \sum^{\text{Oct.}} |\, a_{ij}.a_{ik}|_o^{\,2} + B_c \sum^{\text{Cube}} |\, a_{ij}.a_{ik}|_c^{\,2}}{B_o\, |\, a_{ij}.a_{ik}|_{op}} \gamma_p \qquad (6)$$

where the additional subscript (p) refers to the primary slip system.

In order to reconcile the two parameters B_o and B_c for the two families of octahedral and cube slip systems, respectively, we can qualitatively reason a relationship between them. It is reasonable to expect that the glide of dislocations on one or the other slip system will be controlled by their relative values of CRSS. A system with a higher CRSS is expected to be less active at a given shear stress than a system with a lower CRSS. Thus we can assume that the ratio of these parameters will be inversely proportional to their CRSS values.

That is
$$\frac{B_o}{B_c} = \frac{(CRSS)_{cube}}{(CRSS)_{oct.}} = R \qquad (7)$$

Substituting the Equation (7) into Equation (6) yields the following relationship where only the ratio of CRSS for the two slip systems is unknown but can be easily deduced from experiments.

$$\epsilon_{ii} = \frac{\sum^{Oct.} |a_{ij}.a_{ik}|_o^2 + (1/R) \sum^{Cube} |a_{ij}.a_{ik}|_c^2}{|a_{ij}.a_{ik}|_{op}} \gamma_p \qquad (8)$$

Making a critical assumption that fracture will always occur at an equivalent critical fracture shear strain on the primary octahedral slip system, irrespective of the shear strain distribution or the dominance of the cube or octahedral slip systems, a unified fracture criterion can be deduced from Equation (8). The equation can be expressed in a much more simplified form as follows:

$$\epsilon_f = \frac{\sum^{Oct.} m^2 + (1/R) \sum^{Cube} n^2}{m_p} \gamma_f \qquad (9)$$

where consistent with the notation used in the literature,
m is the Schmid factor for octahedral slip systems , and
n is the Schmid factor for cube slip systems.

At this point it is important to demonstrate that the derived relation satisfies at least certain simple boundary conditions. Consider for example the deformation behavior of an <001> symmetric orientation in the temperature region where the role of cube slip can be ignored, that is, R is very large. Thus the second factor in the numerator can be ignored. In addition, owing to the symmetry, the deformation must occur on eight (8) octahedral slip systems with identical values for the Schmid factor. As a result the relationship extremely simplified, is

$$\epsilon_{<001>f} = 8\, m\, \gamma_f$$

In the absence of any interactions, the expression simply quantifies that for the <001> orientation the total fracture elongation is eight times the resolved fracture shear strain on the primary octahedral slip system.

Having reasonably rationalized the distribution of total elongation in terms of shear strains, we now proceed to account for inter-slip system interactions. To achieve this we assume that dislocation activity on other slip systems effectively reduces the critical fracture shear strain. Once again to assess the activity of various slip systems we use relative resolved shear stresses. Similar reasoning has been used in developing models for the yield strength of $L1_2$ compounds by defining ratios of the Schmid factor for the slip system under consideration to the Schmid factor for the primary slip system. Thus we can express γ_f in terms of a zero interaction critical shear strain value γ_o as follows:

$$\gamma_f = \gamma_o \left[1 - A \left(\frac{| a_{ij} \cdot a_{ik} |_o}{| a_{ij} \cdot a_{ik} |_p} + (1/R) \frac{| a_{ij} \cdot a_{ik} |_c}{| a_{ij} \cdot a_{ik} |_p} \right) \right] \quad (10)$$

Where A is introduced as a single interaction parameter for both octahedral and cube slip systems.

To account for the difference in the intensity of the interaction from the two slip systems, again the ratio of CRSS, R, is introduced. The relationship certainly satisfies the boundary condition where deformation is dominated by octahedral slip and the parameter R is very large, effectively making interaction from cube slip systems insignificant. To retain symmetry, in the summation of interactions from various slip systems the primary slip system is also included. This alters the way the interaction parameter A is evaluated but does not alter the modelling concept *in any significant* way.

Combining the concept of shear strain distribution and the interaction effect, the elongation as a function of orientation can be simply expressed as follows in familiar notation.

$$\epsilon_f = \frac{\sum^{Oct.} m^2 + (1/R) \sum^{Cube} n^2}{m_p} (1 - A (M + (1/R) N)) \gamma_o \quad (11)$$

Where M and N are Schmid factor ratios for all octahedral and cube slip systems to the primary octahedral slip system for the specific tensile orientation.

In the course of developing the model, several simplifying assumptions were made with the objective of introducing only a single parameter. Among these assumptions, however, the most significant one is the concept of critical shear strain for failure. It seems intuitively correct that for a material which does not show extensive necking the failure must occur by a notch formed by accumulation of dislocations at a slip step which may also be affected by dislocations gliding on other interacting slip systems.

In order to test the validity of the model a computer was programmed to calculate relative elongation as a function of orientation within a standard stereographic orientation triangle for a cubic material. For this purpose the zero interaction critical shear strain γ_o was assumed to be unity. The interaction parameter A and ratio of CRSS of cube to octahedral slip systems were

the only input to the program. The output from the program was plotted to represent iso-elongation contours within the orientation triangle.

The ternary alloy Ta-195 was chosen as a realistic and representative system. As shown in Figure 16(c), for this alloy three distinct temperature regions can be identified. At room temperature the ratio of CRSS of cube to octahedral slip systems, R=1.5. That implies that octahedral slip dominates the deformation. At around 700K, where the CRSS curves for cube slip and octahedral slip cross the ratio R=1.0. This is the temperature range at which both systems compete providing highest mutual interaction as well as the largest number of slip systems for strain distribution. At 1000K, where the ratio of CRSS R=0.5, cube slip dominates the deformation. Using the observed values of the parameter R and qualitatively realistic values of the interaction parameter, the three temperature regions were modeled as presented in Figure 31. For room temperature, where R=1.5, strong inter-slip interaction was assumed. With increasing temperature a lower value for the interaction parameter was used, reflecting increased thermal recovery. To some extent, the value of the interaction parameter was contrained by the manner in which the model has been constructed, making it somewhat limited by the value of the parameter, R. Nevertheless the choice of the model parameter is not physically meaningless.

The results from Figure 31 are plotted at three temperatures for the four major orientations in Figure 32. Comparison of Figure 32 with the actual elongation plot for Ta-195 in Figure 22 shows the model to be remarkably successful in predicting the relative elongation as a function of orientation. At room temperature the model correctly predicts the general level and hierarchy of the orientation. The ductility is observed to decrease in the order of <011>, <123>, <001> and <111> and the model prediction completely agrees with the observations. At 700K the ductility is observed to decrease in the order of <001>, <011>, <111> and <123>; and once again the prediction matches the observations. At 1000K the model correctly predicts the <111> to be significantly more ductile than the <001> orientation but the order in which the relative elongations of <123> and <011> are predicted do not match with observations.

It is important to recognize that the plot in Figure 32 entails the assumption of a constant zero interaction critical shear strain for the octahedral slip system, γ_o. If the prediction in Figure 32 were to be matched with the observations in Figure 22, the value of γ_o should be allowed to decrease with increasing temperature. This seem consistent with the increasingly deleterious effect of environment with increasing temperature (Reference 22) leading to some loss of intrinsic ductility. Further undue interpretation of the model is not warranted at this time without additional verification and refinement. It must be noted that we have not considered any effect due to constriction stress or dislocation core structure. With test data available for only four orientations, it was considered statistically meaningless to introduce any more model parameters. It appears that further controlled study of work hardening as a function of orientation in both tension and compression is necessary to provide additional refinement of the model.

Since the model invokes nothing more than the geometry of a cubic single crystal, it can be applied to practical systems such as nickel base

superalloys to normalize the orientation dependence of ductility and further refinement may even allow its application to notch failure, which is critical to engineering applications. The qualitative success of the model suggests that the assumption of failure occurring at a critical shear strain on the operative slip system, irrespective of the state of stress, may be correct.

4.3 Effect of Alloy Composition on Ductility

Perhaps the most difficult feature of the trends to explain in these alloys is the large influence of stoichiometry on ductility levels. Why do ductility values fall to very low values over a compositional range of only three atom percent? One could simply state from the model developed in 4.1 and 4.2 that the strength of inter-slip system interactions increase over these compositional ranges. Work hardening values increase and this certainly supports such a postulate. The fracture modes observed, in which shear failure on slip planes appears to dominate, also support a critical strain accumulation process. Any such hypothesis should be supported by a physical model to explain the changes. We consider the following factors as important in such a model although it is clear that our understanding is far from complete.

The dislocation structures in the alloys studied vary in a systematic way with composition. If we couple these observations with the tension and Compression flow stress asymmetry the main results are summarized in the following table.

Alloy:	Al240	Al250	Al270	Ta195	Ta205	Ta225
Dissociation Scheme:						
Below Tp:	(1)*+(3)	(2)+(3)	(2)	(2)	(2)	(2)
Near Tp & Above:	(2)	(2)	(2)	(2)	(2)	(2)

APB Energy ——————►----------►

Dislocation Core Spreading ——————►+

\+ Deduced from tension-compression yield strength asymmetry
* Conclusive evidence not yet established. -------► Assumed trend.

where (1): CSF/APB-coupled dislocation, (2): APB-coupled dislocations and (3): SISF-coupled dislocations.

The effects of alloying on dislocations features are apparent from the summary table. At low temperatures, a systematic change in dislocation features can be observed in the binary alloys depending on aluminum content/stoichiometry. In Al 240 dislocations tentatively identified as CS/APB type and SISF-coupled dislocations are present. The latter type of dislocations were also present in Al 250 together with APB-coupled dislocations. In alloy Al 270 only APB-coupled dislocations were found independent of temperatures. APB-coupled dislocations are the most common type of dislocations as they are in all the binary alloys at high temperatures and all the tantalum-modified ternary alloys at all temperatures. Some of the important differences between these dislocations appear to be the spacing between the superlattice partials and/or the planarity of the dislocation core which was

deduced from the magnitude of the tension-compression (T-C) yield strength asymmetry (Section 3.2.2). The absence of significant T-C asymmetry in the binary alloys suggest that the dislocation configuratins are planar in the binary alloys. However, there may be significant differences in the spacing of the superlattice dislocations. Unfortunately, we have not measured the spacings of the low temperature dislocations in the binary alloys. However, the presence of wide stacking fault ribbons at low temperatures in Al 240 and Al 250 suggests that the spacing of the SISF-coupled dislocation must be quite large compared with the spacing of the APB-coupled dislocations in Al 270. The larger spacing of the APB-coupled dislocations in Al 240 compared with Al 270 was confirmed by measurements (see Figure 26).

There are possibly two important differences among the APB-coupled dislocations in the tantalum modified alloys. Both of these differences come from indirect evidence. First, the fact that the APB-coupled dislocations in Ta 195 could not be resolved implies either that the spacings are considerably smaller than that observed in Al 270 which is about 3.5 nm or that the concept of planar dislocation configuration is no longer valid. If the first possibility is correct and if one assumes that the increase in aluminum content also increases the APB energy in the ternary alloys, as observed in the binary alloys, then the spacings of the APB-coupled dislocations in Ta 225 are even smaller yet. On the other hand, if one takes the view that the dislocations in the ternary alloys have nonplanar core structures as suggested by the T-C asymmetry observed in these alloys, the dislocations may not be characterized meaningful in terms of spacings, if indeed it could be measured at all. Assuming the magnitude of the T-C asymmetry is a measure of the extent of dislocation core spreading, our results indicate more core spreading in Ta 225 than in Ta 195.

Returning now to the strength of inter-slip system interaction which, as proposed earlier, may be related to the nature of dislocations in the alloy. To make this association one should compare the work hardening behavior of materials with different types of dislocations in a situation in which the deformation and inter-slip interaction in these materials involve the same set of slip systems. An approximation to this situation is the deformation of <001> orientation at room temperature for the binary alloys and Ta 195 in which only the octahedral slip systems are involved as the CRSS ratios for cube to octahedral slip are large in all these cases. From the work hardening data in Figures 20 and 21 the intensities the octahedral inter-slip interaction at room temperature are found to be proportioal to 520, 700 and 1120 for Al 240, Al 250 and Ta 195, respectively. These differences can be correlated with the different types of dislocations found in these alloys: CSF/APB-coupled and SISF coupled dislocations in Al 240, SISF-coupled and APB-coupled dislocations in Al 250 and APB-coupled dislocations in Ta 195. As discussed in Section 4.2 ductility decreases with increasing intensity of inter-slip interactions. Thus the basic differences in the types of dislocation present in Al 240 and Ta 195 may account for the ductility differences in the <001> orientation between these two alloys. Unfortunately, the intensities of octahedral-cube and cube-cube inter-slip interactions cannot be deduced from data available due to premature failure in some of the specimens. However, it is interesting to note the large drop in work hardening and the accompanying increase in ductility in Ta 195 associated with the onset of cube slip (Figures 21 and 22). This observation would indicate lower intensity for cube-cube inter-slip interaction than the other two types of interaction. For further studies of strength of inter-slip interactions it is suggested that compression

testing be used to alleviate brittleness problems in alloys which show strong inter-slip interactions.

5.0 CONCLUSIONS

Based on studies of ductility, strength characteristics and dislocation features in binary and tantalum-modified ternary Ni_3Al alloy single crystals the following conclusions can be made.

1. The intrinsic ductility of Ni_3Al alloys is strongly influenced by the alloy stoichiometry. Aluminum-rich (hyperstoichiometric) alloys are intrinsically brittle.

2. Based on (1) it is futile to seek improvement in ductility of hyper-stoichiometric alloys by grain boundary strengthening using micro-alloying techniques.

3. There is an apparent correlation between the dislocation configurational structure and the intrinsic ductility of an alloy. Dislocations which have more nonplanar core structure (deduced from tension-compression yield strength asymmetry) or closer spacing between the partials as in the case of the hyperstoichiometric alloys tend to result in lower ductility.

4. Based on (3) an alloying direction for improving ductility alloys is to lower the stacking fault energy in Ni_3Al which promotes formation of stacking fault-coupled dislocations with larger spacings.

5. Another important factor which controls ductility in Ni_3Al alloys is the ratio of the critical resolved shear stresses CRSS for $\{111\}\langle 1\bar{1}0\rangle$ octahedral and $\{001\}\langle 1\bar{1}0\rangle$ cube slip. Ductility in Ni_3Al alloys tend to be lower at temperatures when CRSS for octahedral and cube slip are about equal.

6. Substituting tantalum for aluminum or increasing aluminum content in Ni_3Al tends to raise the CRSS for octahedral slip without significantly changing the CRSS for cube slip, thus shifting the temperature of equi-CRSS for cube and octahedral slip to lower temperatures which results in a ductility minimum at lower temperatures.

7. Based on (6) an alloying direction of improving the ductility of the tantalum-modified Ni_3Al alloy at ambient temperatures is to raise the CRSS for cube slip.

8. The rather complex temperature, orientation and compositional dependence of ductility in both the binary and ternary alloys can be related to the probability of inter-slip interactions. This can be assessed by weighing all the octahedral and cube slip systems with the magnitudes of the applied resolved shear stresses and the CRSS for the respective slip system, and strength of the interaction which is considered to be governed the dislocation configurational structure.

9. Based on (8), a semi-quantitative model has been developed which accounts for the temperature and orientation dependence of a tantalum-modified Ni_3Al reasonably well.

10. The current study appears to be the first to conduct systematic studies of tensile ductility in single crystals using four major orientations and over a wide temperature range and attempt to relate the intrinsic ductility of an intermetallic compound to observed plastic flow and dislocation features. As a result of this study significant understanding of ductility behavior in Ni_3Al alloys has been achieved and some alloying directions for ductility improvements emerge. However to isolate the contribution of dislocation core structure to work hardening and therefore ductility, further study of anisotropy of work hardening in both tension and compression is suggested.

ACKNOWLEDGEMENT

The authors would like to thank Dr. M. J. Blackburn for his interest and stimulating discussions throughout the course of this study and critical review of the manuscript. The following persons are also gratefully acknowledged: S. M. Russell for preparation of the manuscript, C. Calverley, R. Londin and J. DeFilippo for their technical assistance.

REFERENCES

1. M. Yamaguchi, V. Paidar, D. P. Pope, and V. Vitek: Philos. Mag. A, 1982, Vol. 45, p. 867.

2. V. Paidar, M. Yamaguchi, D. P. Pope, and V. Vitek: Philos. Mag. A, 1982, Vol. 45, p. 883.

3. J. R. Rice and Thomson: Philos. Mag., 1974, Vol. 29, p. 73.

4. K. Aoki and O. Izumi: J. Japan Inst. Metals, 1979, Vol. 43, pp. 1190-1196.

5. T. Takasugi, N. Masahashi and O. Izumi: Scripta Metall., 1986, Vol. 20, p. 1317.

6. B. H. Kear, A. F. Giamei, J. M. Silcock, and R. K. Ham: Scripta Metall., 1968, Vol. 2, p. 287.

7. B. H. Kear, A. F. Giamei, G. R. Leverant, and J. M. Oblak: Scripta Metall., 1969, Vol. 3, p. 123.

8. B. H. Kear, A. F. Giamei, G. R. Leverant, and J. M. Oblak: Scripta Metall., 1969, Vol. 3, p. 455.

9. D. P. Pope and S. S. Ezz: Int. Metals Rev., 1984, Vol. 29, No. 3, pp. 136-137.

10. Y. Mishima, Y. Oya and T. Suzuki: in High Temperature Ordered Intermetallic Alloys Symposium Proceedings, Materials Research Society 1984 Fall Meeting, Boston, MA.

11. M. J. Marcinkowski, N. Brown and R. M. Fisher: Acta Metall., 1961, Vol. 9, p. 129.

12. K. Aoki and O. Izumi: Acta Metall., 1978, Vol. 26, pp. 1257-1263.

13. K. Aoki and O. Izumi: J. Mater. Sci., 1979, Vol. 14, pp. 1800-1806.

14. K. Aoki and O. Izumi: Acta Metall., 1979, Vol. 27, pp. 807-816.

15. N. S. Stoloff and R. G. Davies: "The Mechanical Properties of Ordered Alloys," Pergamon Press, Oxford, 1966.

16. Y. Umakoshi, D. P. Pope and V. Vitek: Acta Metall., 1984, Vol. 32, No. 3, pp. 449-456.

17. M. Gell, D. N. Duhl and A. F. Giamei: in "Superalloys 1980," Proceedings of the Fourth International Symposium on Superalloys, September 1980, Eds. J. K. Tien, S. T. Wlodek, H. Morrow III, M. Gell, and G. E. Mauer, ASM Publication, pp. 205-214.

18. B. H. Kear, G. R. Leverant, and J. M. Oblak: Trans. ASM, 1969, Vol. 62, p. 639.

19. J. W. Edington: "Practical Electron Microscopy in Materials Science," Van Nostrand Reinhold Co., New York, 1976, p. 148.

20. A. Seeger: in "Work Hardening," Eds. J. P. Hirth and J. Weertman, Gordon and Breach, New York, 1968, pp. 27-63.

21. C. T. Liu, C. L. White and J. A. Horton: Acta Metall., 1985, Vol. 33, p. 213.

22. C. T. Liu, C. L. White and E. H. Lee: Scripta Metall., 1985, Vol. 19, pp. 1247-1250.

23. A. I. Taub, S. C. Huang and K. M. Chang: Metall. Trans. A, 1984, Vol. 15A, p. 399.

24. C. C. Law and M. J. Blackburn: "Rapidly Solidified Alloys for Disk Applications," Air Force Contract No. F33615-83-C-5103, Final Report AFWAL-TR-87-4019, 1987.

25. I. Baker and E. M. Schulson: Phys. Stat. Sol. A, 1985, Vol. 89, pp. 163-172.

26. I. Baker and E. M. Schulson: Phys. Stat. Sol. A, 1984, Vol. 85, pp. 481-490.

27. D. M. March: in "Fracture of Solids," Proc. Int. Conf. AIMME August 1962, Eds. D. C. Drucker and J. J. Gilman.

Table 1

Nominal Compositions of Alloys Selected for Study
(Atomic Percent)

Alloy	Ni	Al	Other
Al-240	Bal.	23.5	-
Al-250	Bal.	25.0	-
Al-270	Bal.	26.5	-
Ta-195	Bal.	18.5	5.0 Ta
Ta-205	Bal.	20.0	5.0 Ta
Ta-225	Bal.	21.5	5.0 Ta
Sn-204	Bal.	19.5	4.0 Sn
Sn-214	Bal.	21.0	4.0 Sn
Sn-234	Bal.	22.5	4.0 Sn

Table 2

Analyzed Alloy Compositions
(Atomic Percent)

Alloy	Ni	Al	Other
Al-240	76.5	23.5	-
Al-250	75.1	24.9	-
Al-270	73.7	26.3	-
Ta-195	76.4	18.6	5.0 Ta
Ta-205	74.7	20.3	5.0 Ta
Ta-225	73.3	21.7	5.0 Ta
Sn-204	75.9	20.1	4.0 Sn
Sn-214	75.8	20.9	3.3 Sn
Sn-234	*	*	*

*Note: Single crystals of this alloy could not be prepared; therefore, this alloy was not studied.

Table 3

Compositions of the Phases in Al-250 and Al-270
(Atomic Percent)

	Ni	Al
Al-250 (Bulk, Nominal)	75	25
Ni_3Al	75.2	24.8
NiAl	64.4	35.6
Al-270 (Bulk, Nominal)	73.5	26.5
Ni_3Al	74.7	25.3
NiAl	62.6	37.4

Table 4

Compositions of the Phases in Sn-214 Single Crystal
(Atomic Percent)

	Ni	Al	Sn
As-Cast			
Phase A	75.7	23.0	1.2
Phase B	72.8	4.9	22.2
Phase C	60.3	2.4	37.2
After 50 hours at 1339K			
Phase A	75.0	23.1	1.9
Phase B	73.5	6.5	20.0
Phase C	62.1	4.5	33.4

Table 5

Composition of the Phases in Ta-225 Single Crystal
(Atomic Percent)

Phase	Ni	Al	Ta
$L1_2$	73.3	21.1	5.6
B2	60.1	39.9	-

Table 6

Fracture Facets in Binary Ni_3Al Alloys

	Al-240		Al-270	
Stress Axis	294K	1033K	294K	1033K
[001]	(111)	(011)	(001)	*
[011]	(001),(010),{110}	(110),($\bar{1}$10),(010)	*	(101)
[111]	(1$\bar{1}$1),(11$\bar{1}$),($\bar{1}$11)	(1$\bar{1}$1),(11$\bar{1}$),($\bar{1}$11)	(1$\bar{1}$1)	(1$\bar{1}$1)
[123]	{110},{111}	{111}	(11$\bar{1}$),(001)	{111}

*Note: Not determined.

Table 7

Tensile Data for Al-240

(a) <001> Oriented Specimens

Al-240 Ingot 5353-05 HT No.60-3-86

Temperature Deg. F	K	Spec. Ident.	Axial Orientation Deg. from <100>	<010>	<001>	Elong. percent	0.2 % Yield Str ksi	MPa	U. T. S. ksi	MPa
		<001>	90	90	0					
70.0	294.1	BA	88.0	87.3	3.4	32.0	14.5	99.7	126.97	875.5
800.0	699.7	BB	90.0	90.0	0.0	28.4	52.2	360.2	131.79	908.7
1,400.0	1,033.0	BC	90.0	90.0	0.0	8.0	125.9	868.3	127.93	882.1
1,600.0	1,144.1	BD	90.0	90.0	0.0	13.8	82.1	566.0	86.43	595.9

			Schmid Factors Octahedral Slip	Cube Slip	Resolved Shear Strength Octahedral Slip Ksi	MPa	Cube Slip Ksi	MPa
		<001>	0.4084	0.0004				
70	294.1	BA	0.4263	0.0583	6.17	42.52	0.84	5.81
800	699.7	BB	0.4084	0.0004	21.33	147.08	0.02	0.15
1,400	1,033.0	BC	0.4084	0.0004	51.43	354.60	0.05	0.36
1,600	1,144.1	BD	0.4084	0.0004	33.52	231.14	0.03	0.24

(b) <011> Oriented Specimens

Al-240 Ingot 5353-05 HT No.60-3-86

Temperature Deg. F	K	Spec. Ident.	Axial Orientation Deg. from <100>	<010>	<001>	Elong. percent	0.2 % Yield Str. ksi	MPa	U. T. S. ksi	MPa
		<011>	90	45	45					
70.0	294.1	AA	87.2	45.7	44.4	69.3	12.9	88.8	86.94	599.4
800.0	699.7	AB	90.0	45.0	45.0	51.3	39.5	272.6	96.06	662.4
1,400.0	1,033.0	AC	90.0	45.0	45.0	8.6	84.1	580.0	88.55	610.5
1,600.0	1,144.1	AD	90.0	45.0	45.0	16.6	68.2	470.0	73.04	503.6

			Schmid Factors Octahedral Slip	Cube Slip	Resolved Shear Strength Octahedral Slip Ksi	MPa	Cube Slip Ksi	MPa
		<011>	0.4085	0.3538				
70	294.1	AA	0.4253	0.3778	5.48	37.76	4.87	33.55
800	699.7	AB	0.4085	0.3538	16.15	111.33	13.99	96.44
1,400	1,033.0	AC	0.4085	0.3538	34.36	236.90	29.76	205.21
1,600	1,144.1	AD	0.4085	0.3538	27.84	191.99	24.12	166.30

Table 7 (continued)

Tensile Data for Al-240

(c) <111> Oriented Specimens

Al-240 Ingot 5353-05 HT No.60-3-86

Temperature Deg. F	K	Spec. Ident.	Axial Orientation Deg. from <100>	<010>	<001>	Elong. percent	0.2 % Yield Str. ksi	MPa	U. T. S. ksi	MPa
		<111>	54.74	54.74	54.74					
70.0	294.1	BA	56.9	53.8	53.6	24.5	16.4	113.2	136.80	943.3
800.0	699.7	BB	56.9	53.8	53.6	17.1	56.4	388.7	187.91	1,295.6
1,400.0	1,033.0	BC	56.9	53.8	53.6	13.1	67.9	468.2	74.33	512.5
1,600.0	1,144.1	BD	56.9	53.8	53.6	15.2	48.1	332.0	65.51	451.7

			Schmid Factors Octahedral Slip	Cube Slip	Resolved Shear Strength Octahedral Slip Ksi	MPa	Cube Slip Ksi	MPa
		<111>	0.2722	0.4715				
70	294.1	BA	0.2969	0.4772	4.87	33.61	7.83	54.02
800	699.7	BB	0.2969	0.4772	16.74	115.40	26.90	185.49
1,400	1,033.0	BC	0.2969	0.4772	20.16	139.01	32.40	223.43
1,600	1,144.1	BD	0.2969	0.4772	14.30	98.57	22.98	158.43

(d) <123> Oriented Specimens

Al-240 Ingot 5353-05 HT No.60-3-86

Temperature Deg. F	K	Spec. Ident.	Axial Orientation Deg. from <100>	<010>	<001>	Elong. percent	0.2 % Yield Str. ksi	MPa	U. T. S. ksi	MPa
		<123>	74.5	57.69	36.7					
70.0	294.1	BA	74.6	59.4	35.0	51.7	11.0	75.6	75.16	518.3
800.0	699.7	BB	74.6	59.4	35.0	33.6	36.9	254.5	89.06	614.1
1,400.0	1,033.0	BC	74.6	59.4	35.0	18.3	79.4	547.5	81.02	558.7
1,600.0	1,144.1	BD	74.6	59.4	35.0	11.0	57.1	393.8	57.11	393.8

			Schmid Factors Octahedral Slip	Cube Slip	Resolved Shear Strength Octahedral Slip Ksi	MPa	Cube Slip Ksi	MPa
		<123>	0.4667	0.4548				
70	294.1	BA	0.4707	0.4489	5.16	35.58	4.92	33.93
800	699.7	BB	0.4707	0.4489	17.37	119.79	16.57	114.25
1,400	1,033.0	BC	0.4707	0.4489	37.38	257.70	35.65	245.79
1,600	1,144.1	BD	0.4707	0.4489	26.88	185.35	25.64	176.79

Table 8

Tensile Data for Al-250

(a) <001> Oriented Specimens

Al-250 Ingot 5210 HT No.60-2-86

Temperature Deg. F	K	Spec. Ident.	Axial Orientation Deg. from <100>	<010>	<001>	Elong. percent	0.2 % Yield Str ksi	MPa	U. T. S. ksi	MPa
		<001>	90	90	0					
70.0	294.1	AD	86.7	85.8	5.4	47.9	20.2	139.3	117.85	812.5
800.0	699.7	AC	86.7	85.8	5.4	24.9	77.4	534.0	154.04	1,062.1
1,400.0	1,033.0	AB	86.7	85.8	5.4	2.6	57.4	395.5	57.35	395.5
1,600.0	1,144.1	AA	86.7	85.8	5.4	6.8	55.2	380.4	59.84	412.6

			Schmid Factors Octahedral Slip	Cube Slip	Resolved Shear Strength Octahedral Slip Ksi	MPa	Cube Slip Ksi	MPa
		<001>	0.4084	0.0004				
70	294.1	AD	0.4364	0.0924	8.82	60.78	1.87	12.87
800	699.7	AC	0.4364	0.0924	33.79	233.00	7.16	49.34
1,400	1,033.0	AB	0.4364	0.0924	25.03	172.56	5.30	36.54
1,600	1,144.1	AA	0.4364	0.0924	24.08	166.00	5.10	35.15

(b) <011> Oriented Specimens

Al-250 Ingot 5210 HT No.60-2-86

Temperature Deg. F	K	Spec. Ident.	Axial Orientation Deg. from <100>	<010>	<001>	Elong. percent	0.2 % Yield Str. ksi	MPa	U. T. S. ksi	MPa
		<011>	90	45	45					
70.0	294.1	AA	88.7	47.8	42.2	47.9	15.4	106.2	77.04	531.2
800.0	699.7	CC	75.1	50.0	43.8	0.6	54.0	372.5	52.31	360.7
1,400.0	1,033.0									
1,600.0	1,144.1	BB	76.7	52.8	40.3	3.8	57.7	398.0	62.81	433.1

			Schmid Factors Octahedral Slip	Cube Slip	Resolved Shear Strength Octahedral Slip Ksi	MPa	Cube Slip Ksi	MPa
		<011>	0.4085	0.3538				
70	294.1	AA	0.4335	0.3640	6.68	46.05	5.61	38.68
800	699.7	CC	0.4644	0.4752	25.09	173.00	25.67	176.99
1,400	1,033.0							
1,600	1,144.1	BB	0.4794	0.4625	27.67	190.78	26.70	184.08

Table 8 (continued)

Tensile Data for Al-250

(c) <111> Oriented Specimens

Al-250 Ingot 5210 HT No.60-2-86

Temperature Deg. F	K	Spec. Ident.	Axial Orientation Deg. from <100>	<010>	<001>	Elong. percent	0.2 % Yield Str. ksi	MPa	U. T. S. ksi	MPa
		<111>	54.74	54.74	54.74					
70.0	294.1	BE	55.1	54.6	54.5	12.6	22.1	152.4	163.20	203.1
800.0	699.7	AB	54.8	54.8	54.6	13.4	89.7	618.5	170.79	1,177.6
1,400.0	1,033.0	AD	54.8	54.8	54.6	0.0	32.8	226.2	79.43	547.6
1,600.0	1,144.1	AA	54.8	54.8	54.6	53.4	54.5	376.0	56.30	388.2

			Schmid Factors Octahedral Slip	Cube Slip	Resolved Shear Strength Octahedral Slip Ksi	MPa	Cube Slip Ksi	MPa
		<111>	0.2722	0.4715				
70	294.1	BE	0.3737	0.5766	11.01	75.92	16.99	117.14
800	699.7	AB	0.3718	0.5778	33.35	229.96	51.83	357.37
1,400	1,033.0	AD	0.3718	0.5778	12.20	84.10	18.96	130.70
1,600	1,144.1	AA	0.3718	0.5778	20.28	139.81	31.51	217.27

(d) <123> Oriented Specimens

Al-250 Ingot 5210 HT No.60-2-86

Temperature Deg. F	K	Spec. Ident.	Axial Orientation Deg. from <100>	<010>	<001>	Elong. percent	0.2 % Yield Str. ksi	MPa	U. T. S. ksi	MPa
		<123>	74.5	57.69	36.7					
70.0	294.1									
800.0	699.7									
1,400.0	1,033.0									
1,600.0	1,144.1									

			Schmid Factors Octahedral Slip	Cube Slip	Resolved Shear Strength Octahedral Slip Ksi	MPa	Cube Slip Ksi	MPa
		<123>	0.4667	0.4548				
70	294.1							
800	699.7							
1,400	1,033.0							
1,600	1,144.1							

Table 9

Tensile Data for Al-270

(a) <001> Oriented Specimens

Al-270 Ingot 5353-04 HT No.60-1-86

Temperature Deg. F	Temperature K	Spec. Ident.	Axial Orientation Deg. from <100>	Axial Orientation Deg. from <010>	Axial Orientation Deg. from <001>	Elong. percent	0.2 % Yield Str ksi	0.2 % Yield Str MPa	U. T. S. ksi	U. T. S. MPa
		<001>	90	90	0					
70.0	294.1	BC	86.8	81.9	8.8	3.8	25.4	175.3	33.90	233.7
800.0	699.7	AB	89.9	85.8	3.6	1.9	69.6	479.7	70.45	485.6
1,400.0	1,033.0	AA	89.9	85.8	3.6	5.5	44.2	305.1	76.11	524.8
1,600.0	1,144.1	BD	86.8	81.9	8.8					

			Schmid Factors Octahedral Slip	Schmid Factors Cube Slip	Resolved Shear Strength Octahedral Slip Ksi	Resolved Shear Strength Octahedral Slip MPa	Resolved Shear Strength Cube Slip Ksi	Resolved Shear Strength Cube Slip MPa
		<001>	0.4084	0.0004				
70	294.1	BC	0.4576	0.1375	11.63	80.21	3.50	24.10
800	699.7	AB	0.4370	0.0542	30.40	209.63	3.77	25.99
1,400	1,033.0	AA	0.4370	0.0542	19.34	133.34	2.40	16.53
1,600	1,144.1	BD	0.4576	0.1375				

(b) <011> Oriented Specimens

Al-270 Ingot 5353-04 HT No.60-1-86

Temperature Deg. F	Temperature K	Spec. Ident.	Axial Orientation Deg. from <100>	Axial Orientation Deg. from <010>	Axial Orientation Deg. from <001>	Elong. percent	0.2 % Yield Str. ksi	0.2 % Yield Str. MPa	U. T. S. ksi	U. T. S. MPa
		<011>	90	45	45					
70.0	294.1	AD	87.0	46.1	44.0	16.6	22.3	153.5	80.89	557.8
800.0	699.7	AC	87.0	46.1	44.0	8.1	88.5	610.2	114.68	790.7
1,400.0	1,033.0	AB	87.0	46.1	44.0	1.3	44.9	309.5	44.89	309.5
1,600.0	1,144.1	AA	87.0	46.1	44.0	4.1	42.4	292.6	47.96	330.7

			Schmid Factors Octahedral Slip	Schmid Factors Cube Slip	Resolved Shear Strength Octahedral Slip Ksi	Resolved Shear Strength Octahedral Slip MPa	Resolved Shear Strength Cube Slip Ksi	Resolved Shear Strength Cube Slip MPa
		<011>	0.4085	0.3538				
70	294.1	AD	0.4288	0.3796	9.54	65.80	8.45	58.25
800	699.7	AC	0.4288	0.3796	37.95	261.64	33.59	231.60
1,400	1,033.0	AB	0.4288	0.3796	19.25	132.73	17.04	117.49
1,600	1,144.1	AA	0.4288	0.3796	18.20	125.48	16.11	111.07

Table 9 (continued)

Tensile Data for Al-270

(c) <111> Oriented Specimens

Al-270 Ingot 5353-04 HT No.60-1-86

Temperature Deg. F	K	Spec. Ident.	Axial Orientation Deg. from <100>	<010>	<001>	Elong. percent	0.2 % Yield Str. ksi	MPa	U. T. S. ksi	MPa
		<111>	54.74	54.74	54.74					
70.0	294.1	AC	61.2	54.3	49.2	10.7	37.5	258.9	47.38	326.7
800.0	699.7	BF	52.5	53.4	58.4	0.5			79.90	550.9
1,400.0	1,033.0	AA	61.2	54.3	49.2	3.1	33.6	231.9	38.18	263.3
1,600.0	1,144.1	AD	61.2	54.3	49.2	60.0	21.6	148.6	22.41	154.5

			Schmid Factors Octahedral Slip	Cube Slip	Resolved Shear Strength Octahedral Slip Ksi	MPa	Cube Slip Ksi	MPa
		<111>	0.2722	0.4715				
70	294.1	AC	0.3505	0.4928	13.16	90.72	18.50	127.56
800	699.7	BF	0.2367	0.4467				
1,400	1,033.0	AA	0.3505	0.4928	11.79	81.28	16.58	114.29
1,600	1,144.1	AD	0.3505	0.4928	7.55	52.08	10.62	73.23

(d) <123> Oriented Specimens

Al-270 Ingot 5353-04 HT No.60-1-86

Temperature Deg. F	K	Spec. Ident.	Axial Orientation Deg. from <100>	<010>	<001>	Elong. percent	0.2 % Yield Str. ksi	MPa	U. T. S. ksi	MPa
		<123>	74.5	57.69	36.7					
70.0	294.1	AC	74.8	59.0	35.3	43.3	17.0	117.1	82.34	567.7
800.0	699.7	AB	74.6	59.4	35.3	3.8	56.4	389.0	56.42	389.0
1,400.0	1,033.0	AA	74.6	59.4	35.3	6.1	76.6	528.2	38.10	262.7
1,600.0	1,144.1	AD	74.6	59.4	35.3	20.1	35.2	242.6	60.26	415.5

			Schmid Factors Octahedral Slip	Cube Slip	Resolved Shear Strength Octahedral Slip Ksi	MPa	Cube Slip Ksi	MPa
		<123>	0.4667	0.4548				
70	294.1	AC	0.4706	0.4486	7.99	55.08	7.62	52.51
800	699.7	AB	0.4681	0.4473	26.41	182.12	25.24	174.02
1,400	1,033.0	AA	0.4681	0.4473	35.86	247.26	34.27	236.27
1,600	1,144.1	AD	0.4681	0.4473	16.47	113.58	15.74	108.53

Table 10

Tensile Data for Ta-195

(a) <001> Oriented Specimens

Temperature Deg. F	K	Spec. Ident.	Axial Orientation Deg. from <100>	<010>	<001>	Elong. percent	0.2 % Yield Str ksi	MPa	U. T. S. ksi	MPa
		<001>	90	90	0					
70.0	294.1	BA	90.0	81.1	8.9	12.0	57.9	399.2	104.5	720.5
70.0	294.1	CE	89.5	81.2	8.9	21.3	62.1	428.2	101.1	697.1
800.0	699.7	CG	89.5	81.2	8.9	25.4	108.0	744.7	122.1	841.9
800.0	699.7	.	.	.	.	.	.	.	.	.
1400.0	1,033.0	BD	90.0	81.1	8.9	10.6	117.5	810.2	146.3	1008.7
1400.0	1,033.0	CF	89.5	81.2	8.9	13.0	133.2	918.4	152.7	1052.9
1600.0	1,144.1	.	.	.	.	.	.	.	.	.
1600.0	1,144.1	.	.	.	.	.	.	.	.	.

			Schmid Factors Octahedral Slip	Cube Slip	Resolved Shear Strength Octahedral Slip Ksi	MPa	Cube Slip Ksi	MPa
		<001>	0.4084	0.0004				
70.0	294.1	BA	0.4610	0.1091	26.69	184.04	6.32	43.54
70.0	294.1	CE	0.4612	0.1135	28.64	197.47	7.05	48.60
800.0	699.7	CG	0.4612	0.1135	49.81	343.43	12.26	84.51
800.0	699.7	.	.	.	.	.	.	.
1400.0	1033.0	BD	0.4610	0.1091	54.17	373.48	12.82	88.37
1400.0	1033.0	CF	0.4612	0.1135	61.43	423.56	15.12	104.23
1600.0	1144.1	.	.	.	.	.	.	.
1600.0	1144.1	.	.	.	.	.	.	.

(b) <011> Oriented Specimens

Temperature Deg. F	K	Spec. Ident.	Axial Orientation Deg. from <100>	<010>	<001>	Elong. percent	0.2 % Yield St ksi	MPa	U. T. S. ksi	MPa
		<011>	90	45	45					
70.0	294.1	BE	84.5	47.9	42.6	28.2	57.5	396.5	97.9	675.0
70.0	294.1	AB	86.3	45.7	44.6	22.0	42.5	293.0	95.6	659.2
800.0	699.7	BF	84.5	47.9	42.6	21.1	101.8	701.9	115.7	797.8
800.0	699.7	AA	86.3	45.7	44.6	24.6	98.1	676.4	119.1	821.2
1400.0	1,033.0	BG	84.5	47.9	42.6	30.0	98.4	678.5	123.6	852.2
1400.0	1,033.0	AC	86.3	45.7	44.6	23.5	87.5	603.3	120.5	830.8
1600.0	1,144.1	BH	84.5	47.9	42.6	20.1	.	.	100.4	692.3
1600.0	1,144.1	AD	86.3	45.7	44.6	13.7	57.6	397.2	96.9	668.1

			Schmid Factors Octahedral Slip	Cube Slip	Resolved Shear Strength Octahedral Slip Ksi	MPa	Cube Slip Ksi	MPa
		<011>	0.4085	0.3538				
70.0	294.1	BE	0.4452	0.3989	25.60	176.51	22.94	158.15
70.0	294.1	AB	0.4272	0.3848	18.16	125.18	16.35	112.75
800.0	699.7	BF	0.4452	0.3989	45.32	312.49	40.61	279.99
800.0	699.7	AA	0.4272	0.3848	41.91	288.95	37.75	260.25
1400.0	1033.0	BG	0.4452	0.3989	43.81	302.06	39.25	270.64
1400.0	1033.0	AC	0.4272	0.3848	37.38	257.73	33.67	232.13
1600.0	1144.1	BH	0.4452	0.3989	.	.	.	.
1600.0	1144.1	AD	0.4272	0.3848	24.61	169.66	22.16	152.81

Table 10 (continued)

Tensile Data for Ta-195

(c) <111> Oriented Specimens

Temperature Deg. F	K	Spec. Ident.	Axial Orientation Deg. from <100>	<010>	<001>	Elong. percent	0.2 % Yield St ksi	MPa	U. T. S. ksi	MPa
		<111>	54.74	54.74	54.74					
70.0	294.1	BE	61.1	52.6	50.9	3.7	91.9	633.7	173.3	1194.9
70.0	294.1	AA	57.0	55.5	51.8	3.4	62.7	432.3	123.2	849.5
800.0	699.7	BH	61.1	52.6	50.9	14.3	130.9	902.6	177.9	1226.6
800.0	699.7	AD	57.0	55.5	51.8	22.8	121.8	839.8	163.0	1123.9
1400.0	1,033.0	BG	61.1	52.6	50.9	45.5	79.8	550.2	109.7	756.4
1400.0	1,033.0	AC	57.0	55.5	51.8	60.7	74.1	510.9	105.3	726.0
1600.0	1,144.1	BF	61.1	52.6	50.9	40.1	66.9	461.3	85.0	586.1
1600.0	1,144.1	.	.	.	.	.	.	.	.	.

			Schmid Factors Octahedral Slip	Cube Slip	Resolved Shear Strength Octahedral Slip Ksi	MPa	Cube Slip Ksi	MPa
		<111>	0.2722	0.4715				
70.0	294.1	BE	0.3432	0.4863	31.54	217.46	44.69	308.16
70.0	294.1	AA	0.3036	0.4857	19.04	131.26	30.45	209.97
800.0	699.7	BH	0.3432	0.4863	44.92	309.74	63.66	438.93
800.0	699.7	AD	0.3036	0.4857	36.98	254.99	59.16	407.89
1400.0	1033.0	BG	0.3432	0.4863	27.39	188.83	38.81	267.59
1400.0	1033.0	AC	0.3036	0.4857	22.50	155.13	35.99	248.15
1600.0	1144.1	BF	0.3432	0.4863	22.96	158.30	32.54	224.33
1600.0	1144.1	.	.	.	.	.	.	.

(d) <123> Oriented Specimens

Temperature Deg. F	K	Spec. Ident.	Axial Orientation Deg. from <100>	<010>	<001>	Elong. percent	0.2 % Yield St ksi	MPa	U. T. S. ksi	MPa
		<123>	74.5	57.69	36.7					
70.0	294.1	AB	75.6	52.6	41.1	15.1	56.1	386.8	102.2	704.7
70.0	294.1	BE	76.1	55.1	38.4	20.3	59.5	410.3	109.1	752.2
800.0	699.7	AC	75.6	52.6	41.1	15.6	100.0	689.5	123.0	848.1
800.0	699.7	BF	76.1	55.1	38.4	15.5	111.9	771.6	136.8	943.2
1400.0	1,033.0	AD	75.6	52.6	41.1	39.0	80.0	551.6	92.7	639.2
1400.0	1,033.0	BG	76.1	55.1	38.4	46.7	87.5	603.3	94.6	652.3
1600.0	1,144.1	AA	75.6	52.6	41.1	23.3	61.8	426.1	77.8	536.4
1600.0	1,144.1	BH	76.1	55.1	38.4	45 3	68.5	472.3	74.7	515.1

			Schmid Factors Octahedral Slip	Cube Slip	Resolved Shear Strength Octahedral Slip Ksi	MPa	Cube Slip Ksi	MPa
		<123>	0.4667	0.4548				
70.0	294.1	AB	0.4554	0.4569	25.55	176.15	25.63	176.74
70.0	294.1	BE	0.4666	0.4507	27.76	191.43	26.82	184.90
800.0	699.7	AC	0.4554	0.4569	45.54	313.99	45.69	315.04
800.0	699.7	BF	0.4666	0.4507	52.22	360.03	50.43	347.74
1400.0	1033.0	AD	0.4554	0.4569	36.43	251.19	36.55	252.04
1400.0	1033.0	BG	0.4666	0.4507	40.83	281.52	39.44	271.91
1600.0	1144.1	AA	0.4554	0.4569	28.14	194.04	28.24	194.70
1600.0	1144.1	BH	0.4666	0.4507	31.96	220.39	30.87	212.87

Table 11

Tensile Data for Ta-205

(a) <001> Oriented Specimens

Ta-205-1 Ingot 5200 HT No. 104-1-86

Temperature Deg. F	K	Spec. Ident.	Axial Orientation Deg. from <100>	<010>	<001>	Elong. percent	0.2 % Yield Str ksi	MPa	U. T. S. ksi	MPa
		<001>	90	90	0					
70.0	294.1	AA	89.5	88.6	1.4	0.0	122.5	844.8	150.41	1,037.1
800.0	699.7	AC	89.5	88.6	1.4	0.0	178.9	1,233.3	182.93	1,261.3
1,400.0	1,033.0	AD	89.5	88.6	1.4	9.5	193.0	1,330.6	197.09	1,359.0
1,600.0	1,144.1	BE	88.1	86.5	3.9	22.1	102.6	707.6	108.69	749.4

			Schmid Factors Octahedral Slip	Cube Slip	Resolved Shear Strength Octahedral Slip Ksi	MPa	Cube Slip Ksi	MPa
		<001>	0.4084	0.0004				
70	294.1	AA	0.4182	0.0239	51.24	353.27	2.92	20.15
800	699.7	AC	0.4182	0.0239	74.79	515.69	4.27	29.42
1,400	1,033.0	AD	0.4182	0.0239	80.70	556.41	4.60	31.74
1,600	1,144.1	BE	0.4317	0.0669	44.31	305.49	6.86	47.31

(b) <011> Oriented Specimens

Ta-205-1 Ingot 5200 HT No. 104-1-86

Temperature Deg. F	K	Spec. Ident.	Axial Orientation Deg. from <100>	<010>	<001>	Elong. percent	0.2 % Yield Str. ksi	MPa	U. T. S. ksi	MPa
		<011>	90	45	45					
70.0	294.1	CA	90.0	45.6	44.4	1.4	100.8	695.2	120.66	832.0
800.0	699.7	CB	90.0	45.6	44.4	4.5	136.0	937.7	144.40	995.6
1,400.0	1,033.0	CC	90.0	45.6	44.4	8.8	122.8	846.5	133.74	922.1
1,600.0	1,144.1	CD	90.0	45.6	44.4	22.0	83.9	578.5	86.35	595.4

			Schmid Factors Octahedral Slip	Cube Slip	Resolved Shear Strength Octahedral Slip Ksi	MPa	Cube Slip Ksi	MPa
		<011>	0.4085	0.3538				
70	294.1	CA	0.4127	0.3537	41.61	286.90	35.67	245.91
800	699.7	CB	0.4127	0.3537	56.12	386.98	48.11	331.70
1,400	1,033.0	CC	0.4127	0.3537	50.66	349.32	43.43	299.42
1,600	1,144.1	CD	0.4127	0.3537	34.63	238.74	29.68	204.64

Table 11 (continued)

Tensile Data for Ta-205

(c) <111> Oriented Specimens

Ta-205-1 Ingot 5200 HT No. 104-1-86

Temperature Deg. F	K	Spec. Ident.	Axial Orientation Deg. from <100>	<010>	<001>	Elong. percent	0.2 % Yield Str. ksi	MPa	U. T. S. ksi	MPa
		<111>	54.74	54.74	54.74					
70.0	294.1	BA	62.8	51.2	50.9	1.4	118.3	815.9	123.91	854.3
800.0	699.7	BB	62.8	51.2	50.9	1.7	92.0	634.5	92.02	634.5
1,400.0	1,033.0	BC	62.8	51.2	50.9	2.7	85.9	592.0	96.38	664.5
1,600.0	1,144.1	BD	62.8	51.2	50.9	29.0	69.9	482.0	74.10	510.9

			Schmid Factors Octahedral Slip	Cube Slip	Resolved Shear Strength Octahedral Slip Ksi	Octahedral Slip MPa	Cube Slip Ksi	Cube Slip MPa
		<111>	0.2722	0.4715				
70	294.1	BA	0.3555	0.4837	42.07	290.09	57.23	394.63
800	699.7	BB	0.3555	0.4837	32.72	225.58	44.51	306.87
1,400	1,033.0	BC	0.3555	0.4837	30.53	210.48	41.53	286.33
1,600	1,144.1	BD	0.3555	0.4837	15.58	107.43	21.20	146.15

(d) <123> Oriented Specimens

Ta-205-1 Ingot 5200 HT No. 104-1-86

Temperature Deg. F	K	Spec. Ident.	Axial Orientation Deg. from <100>	<010>	<001>	Elong. percent	0.2 % Yield Str. ksi	MPa	U. T. S. ksi	MPa
		<123>	74.5	57.69	36.7					
70.0	294.1	BA	74.6	60.3	34.2	6.7	98.6	679.7	126.06	869.2
800.0	699.7	BB	74.6	60.3	34.2	8.3	134.4	926.9	154.92	1,068.2
1,400.0	1,033.0	BC	74.6	60.3	34.2	28.0	92.7	639.0	102.44	706.3
1,600.0	1,144.1	BD	74.6	60.3	34.2	35.0	73.2	504.5	74.80	515.7

			Schmid Factors Octahedral Slip	Cube Slip	Resolved Shear Strength Octahedral Slip Ksi	Octahedral Slip MPa	Cube Slip Ksi	Cube Slip MPa
		<123>	0.4667	0.4548				
70	294.1	BA	0.4714	0.4453	46.48	320.45	43.90	302.72
800	699.7	BB	0.4714	0.4453	63.37	436.95	59.86	412.77
1,400	1,033.0	BC	0.4714	0.4453	43.69	301.26	41.27	284.59
1,600	1,144.1	BD	0.4714	0.4453	34.49	237.84	32.59	224.68

Table 12

Tensile Data for Ta-225

(a) <001> Oriented Specimens

Ta-225-1 Ingot 5196 HT No. 104-3-86

Temperature Deg. F	K	Spec. Ident.	Axial Orientation Deg. from <100>	<010>	<001>	Elong. percent	0.2 % Yield Str ksi	MPa	U. T. S. ksi	MPa
		<001>	90	90	0					
70.0	294.1	AA	89.8	89.7	0.4	1.3	137.3	946.7	137.30	946.7
800.0	699.7	AB	89.8	89.7	0.4	0.0	190.7	1,314.7	190.68	1,314.7
1,400.0	1,033.0	AC	89.8	89.7	0.4	0.6	183.7	1,266.4	185.31	1,277.7
1,600.0	1,144.1	AD	89.8	89.7	0.4	11.1	92.1	634.9	99.55	686.4

			Schmid Factors Octahedral Slip	Cube Slip	Resolved Shear Strength Octahedral Slip Ksi	MPa	Cube Slip Ksi	MPa
		<001>	0.4084	0.0004				
70	294.1	AA	0.4106	0.0063	56.37	388.67	0.87	6.00
800	699.7	AB	0.4106	0.0063	78.29	539.79	1.21	8.34
1,400	1,033.0	AC	0.4106	0.0063	75.41	519.95	1.16	8.03
1,600	1,144.1	AD	0.4106	0.0063	37.81	260.68	0.58	4.03

(b) <011> Oriented Specimens

Ta-225-1 Ingot 5196 HT No. 104-3-86

Temperature Deg. F	K	Spec. Ident.	Axial Orientation Deg. from <100>	<010>	<001>	Elong. percent	0.2 % Yield Str. ksi	MPa	U. T. S. ksi	MPa
		<011>	90	45	45					
70.0	294.1	AA	87.7	45.1	45.0	2.4	111.2	767.0	125.46	865.0
800.0	699.7	AB	87.7	45.1	45.0	2.4	151.3	1,042.9	153.79	1,060.4
1,400.0	1,033.0	AC	87.7	45.1	45.0	0.8	100.2	690.9	100.20	690.9
1,600.0	1,144.1	AD	87.7	45.1	45.0	0.8	70.2	484.1	77.14	531.9

			Schmid Factors Octahedral Slip	Cube Slip	Resolved Shear Strength Octahedral Slip Ksi	MPa	Cube Slip Ksi	MPa
		<011>	0.4085	0.3538				
70	294.1	AA	0.4192	0.3737	46.63	321.52	41.58	286.67
800	699.7	AB	0.4192	0.3737	63.41	437.18	56.53	389.79
1,400	1,033.0	AC	0.4192	0.3737	42.00	289.61	37.45	258.22
1,600	1,144.1	AD	0.4192	0.3737	29.43	202.91	26.24	180.92

Table 12 (continued)

Tensile Data for Ta-225

(c) <111> Oriented Specimens

Ta-225-1 Ingot 5196 HT No. 104-3-86

Temperature Deg. F	Temperature K	Spec. Ident.	Axial Orientation Deg. from <100>	<010>	<001>	Elong. percent	0.2 % Yield Str. ksi	MPa	U. T. S. ksi	MPa
		<111>	54.74	54.74	54.74					
70.0	294.1	BA	56.1	55.7	52.3	2.4	144.7	997.8	180.89	1,247.3
800.0	699.7	BB	56.1	55.7	52.3	1.3	142.3	981.0	144.72	997.8
1,400.0	1,033.0	BC	56.1	55.7	52.3	9.2	101.4	699.2	124.56	858.8
1,600.0	1,144.1	BD	56.1	55.7	52.3	12.0	72.6	500.4	74.60	514.3

			Schmid Factors Octahedral Slip	Cube Slip	Resolved Shear Strength Octahedral Slip Ksi	MPa	Cube Slip Ksi	MPa
		<111>	0.2722	0.4715				
70	294.1	BA	0.2948	0.4851	42.66	294.17	70.20	484.03
800	699.7	BB	0.2948	0.4851	41.94	289.21	69.02	475.88
1,400	1,033.0	BC	0.2948	0.4851	29.90	206.13	49.19	339.17
1,600	1,144.1	BD	0.2948	0.4851	21.40	147.54	35.21	242.76

(d) <123> Oriented Specimens

Ta-225-1 Ingot 5196 HT No. 104-3-86

Temperature Deg. F	Temperature K	Spec. Ident.	Axial Orientation Deg. from <100>	<010>	<001>	Elong. percent	0.2 % Yield Str. ksi	MPa	U. T. S. ksi	MPa
		<123>	74.5	57.69	36.7					
70.0	294.1	A1A	75.9	56.9	36.8	4.0	107.6	741.8	124.83	860.7
800.0	699.7	A1B	75.9	56.9	36.8	2.2	139.1	959.1	155.24	1,070.4
1,400.0	1,033.0	B1C	76.3	57.2	36.2	4.3	112.0	772.2	122.00	841.2
1,600.0	1,144.1	B1D	76.3	57.2	36.2	23.3	72.6	500.4	69.76	481.0

			Schmid Factors Octahedral Slip	Cube Slip	Resolved Shear Strength Octahedral Slip Ksi	MPa	Cube Slip Ksi	MPa
		<123>	0.4667	0.4548				
70	294.1	A1A	0.4711	0.4479	50.68	349.45	48.18	332.22
800	699.7	A1B	0.4711	0.4479	65.53	451.82	62.30	429.54
1,400	1,033.0	B1C	0.4737	0.4441	53.05	365.78	49.74	342.94
1,600	1,144.1	B1D	0.4737	0.4441	34.38	237.04	32.23	222.24

Table 13

Comparision of Tension/Compression Asymmetry in Binary and Ternary Alloys

	Alloys							
	Al-240		Al-270		Ta-195		Ta-225	
Orientation/Stress	Temperature							
	294K	700K	294K	700K	294K	700K	294K	700K
	0.2 % Yield Strength, MPa							
<001>Compression	89.6	265.5	245.5	651.6	405.4	781.2	823.3	1,132.8
<001>Tension	100.0	359.9	175.1	479.9	413.7	744.7	945.3	1,314.9
<011>Compression	43.2	393.7	243.4	593.7	542.6	950.8	1,227.3	1,232.1
<011>Tension	88.9	272.4	153.8	610.2	344.8	689.5	766.7	1,043.2

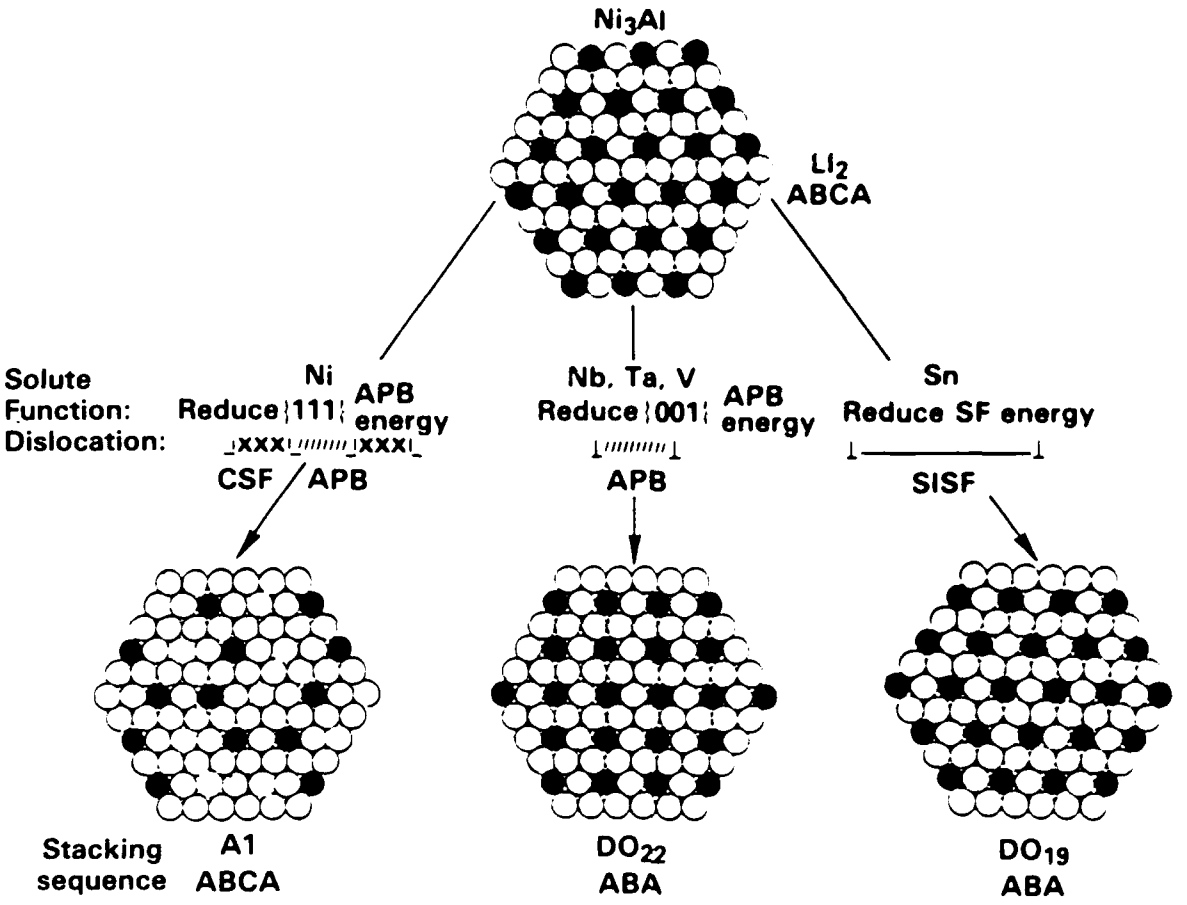

Figure 1 Schematic Diagram Summarizing the Effects of Various Solute Elements on Lattice Stability of the $L1_2$ Structure and the Likely Types of Dislocation Dissociation which Would Occur. The distribution of the solute atoms on the close-packed planes of various derivative structures and their stacking sequence are also depicted.

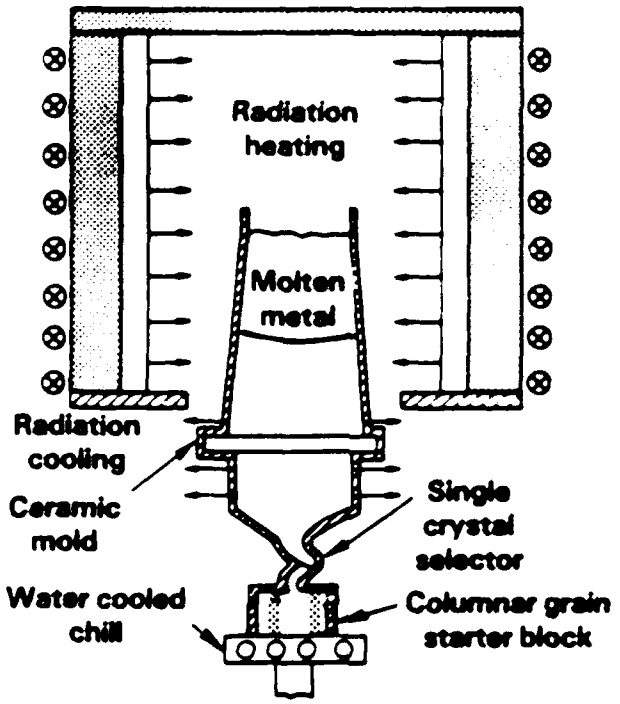

Figure 2 Schematic Diagram of the Directional Solidification Process for Growth of Single Crystals

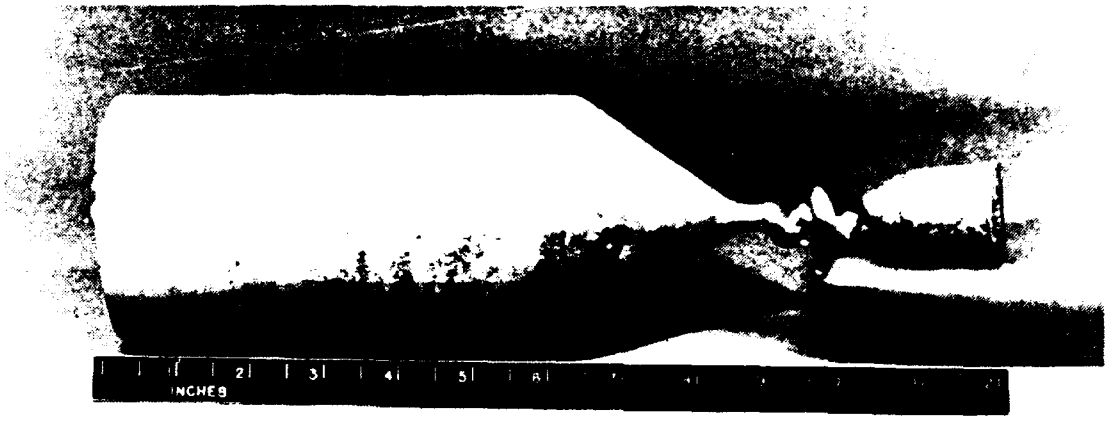

Figure 3 Appearance of a Single Crystal Ingot Removed from the Shell Mold

```
AL 240
INPUT:
     001              210
          TOP
  0.6   10.7 -20.3   -7.9
 -2.2   11.5  15.9   -9.3
 -0.6   13.7  17.6   -6.3
 -1.4   12.7  17.0   -7.8
  1.5   12.1  19.4   -8.4
  1.1   15.5  19.7   -4.7
       BOTTOM
  1.0  -11.1 -19.1    7.9
  1.0  -10.4  18.7   11.0
  1.1  -10.7  18.4    9.9
  0.6  -10.7  18.1   10.3
  1.4  -10.7  18.7   10.3

ALPHA1   ALPHA2   ALPHA3
---------------------------
 11.8     81.6     88.8


MAX ROTATION FROM
AVERAGE ORIENTATION  4.4
IH0001A PAUSE <CR>.....
.
```

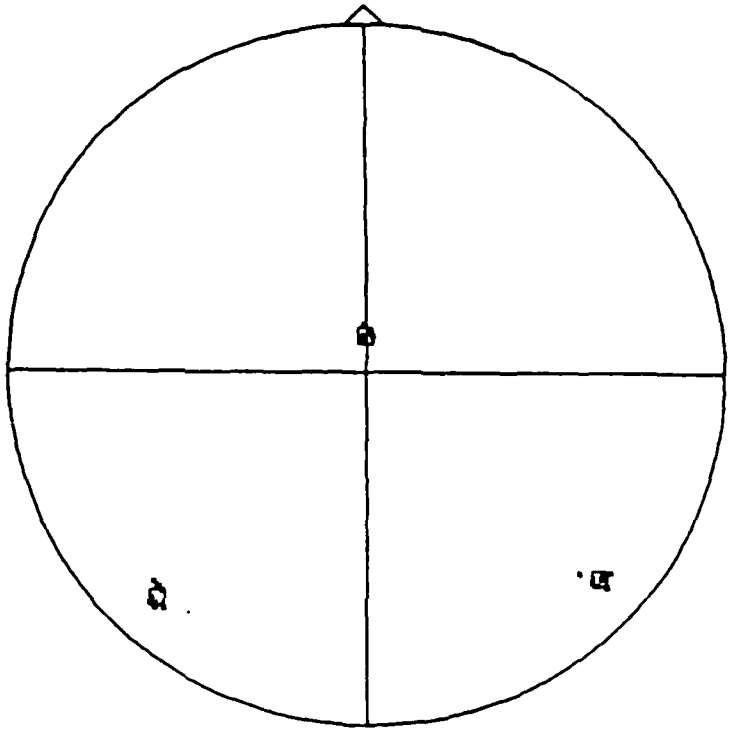

Figure 4 Distribution of <001> Directions on Various Locations on the Top and Bottom Faces of the Single Crystal Ingot of Alloy Al-240 with Reference to Three Orthogonal Axes Chosen to be Parallel to the Axis of the Ingot and the Dendrite Arm Directions

TA-195-1
INPUT:

001		210	
	TOP		
-2.3	-7.7	-1.9	19.8
-2.2	-6.6	-1.8	20.5
-2.4	-6.1	-2.3	21.3
-9.2	3.1	18.1	3.4
-8.1	2.8	18.6	3.2
-4.8	2.8	22.9	3.0
4.8	3.9	-22.9	2.4
3.6	3.7	-23.7	2.3
4.8	2.7	-22.1	1.0
-4.7	8.8	-3.2	-17.9
	BOTTOM		
-2.9	-0.6	24.2	-1.0
-3.0	-1.0	-2.7	25.9
-2.7	0.7	24.5	-0.2
-5.7	-1.2	22.2	-1.6
-5.4	-3.2	21.5	-2.5

ALPHA1	ALPHA2	ALPHA3
2.8	87.4	89.2

MAX.ROTATION FROM
AVERAGE ORIENTATION: 8.7
IH0001A PAUSE <CR>.....

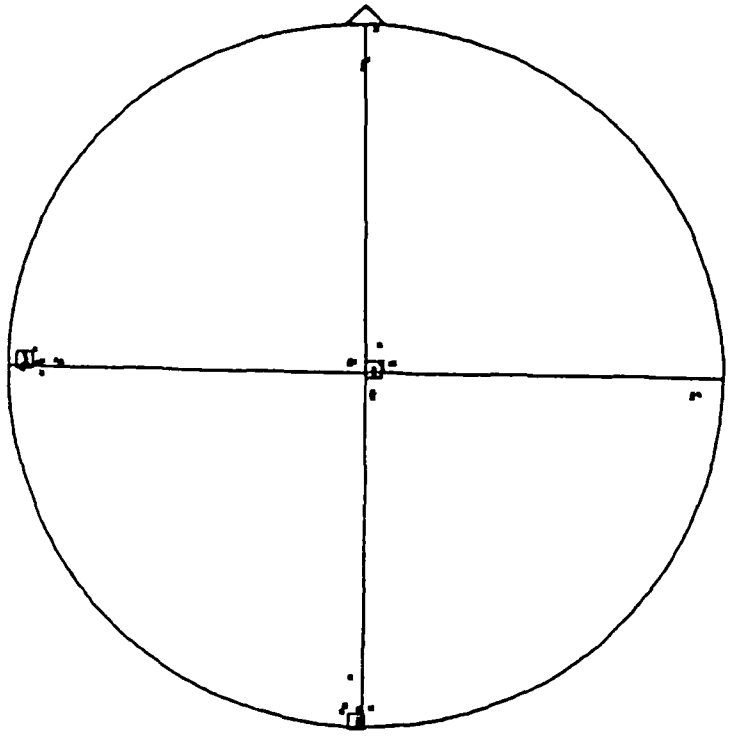

Figure 5 Distribution of <001> Directions on Various Locations on the Top and Bottom Faces of the Single Crystal Ingot of Alloy Ta-195 with Reference to Three Orthogonal Axes Chosen to be Parallel to the Axis of the Ingot and the Dendrite Arm Directions

SN204
INPUT:

011		111	
	TOP		
12.2	0.0	-2.5	-32.2
4.0	-0.5	-8.8	-32.
2.5	-5.5	13.3	28.7
13.0	-7.9	23.9	28.2
	BOTTOM		
11.7	-2.9	-1.3	30.9
3.3	6.8	15.6	-26.8
11.7	6.5	23.5	-28.0
9.7	14.1	21.5	-20.3

ALPHA1	ALPHA2	ALPHA3
35.4	54.8	88.8

MAX. ROTATION FROM
AVERAGE ORIENTATION: 9.3
IH0001A PAUSE <CR>.....
.

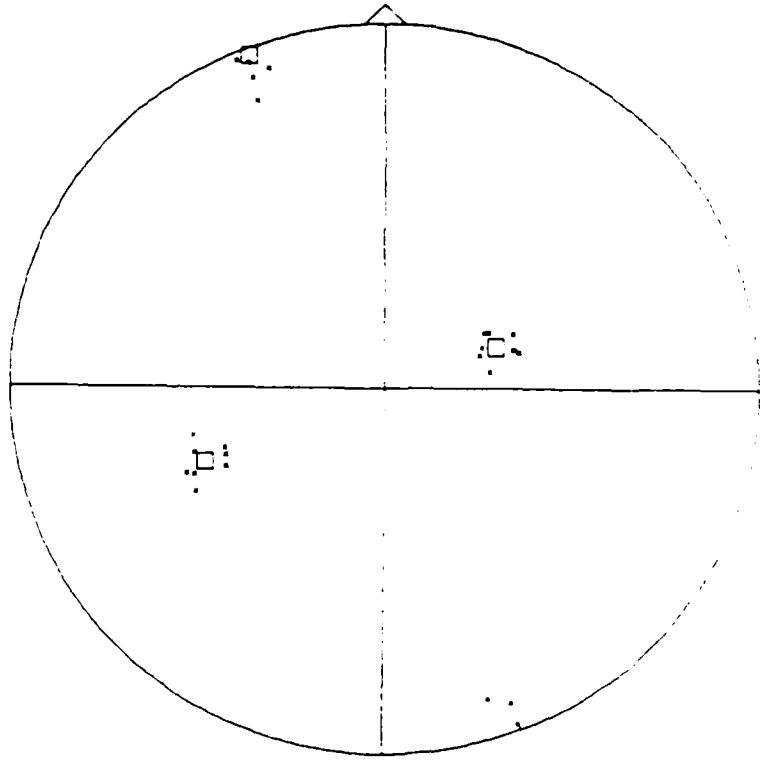

Figure 6 Distribution of <001> Directions on Various Locations on the Top and Bottom Faces of the Single Crystal Ingot of Alloy Sn-204 with Reference to Three Orthogonal Axes Chosen to be Parallel to the Axis of the Ingot and the Dendrite Arm Directions

Figure 7 Appearance of a Crystal Section After Cylindrical Slugs with Different Crystallographic Orientations have been Removed by EDM Technique. X-ray orientation measurements were made on five different locations (the smaller, circular regions) on each end of the ingot.

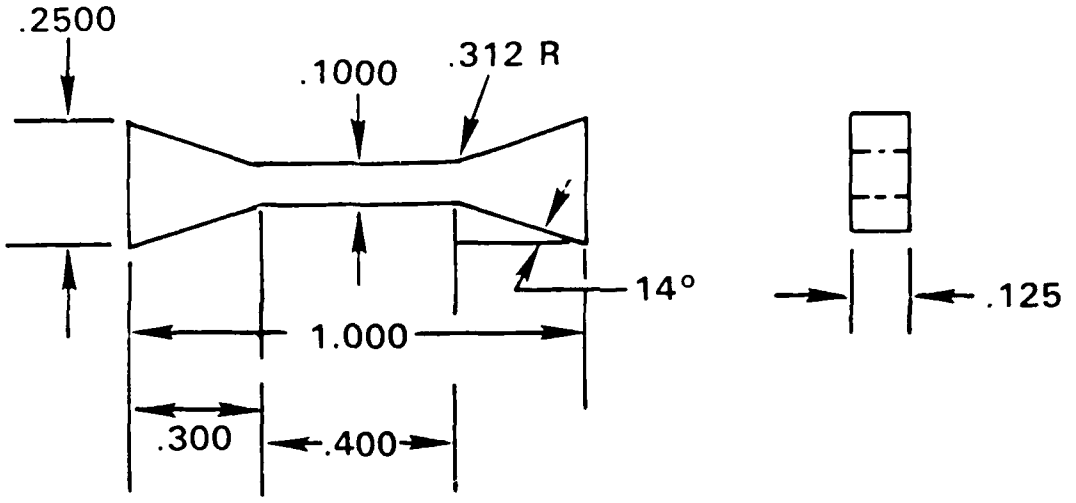

Figure 8 Diagram of the Tensile Specimen Used for the Current Studies (dimensions in inches)

Figure 9 Microstructure of Al-240 in the As-Cast Condition. The dark phase is NiAl.

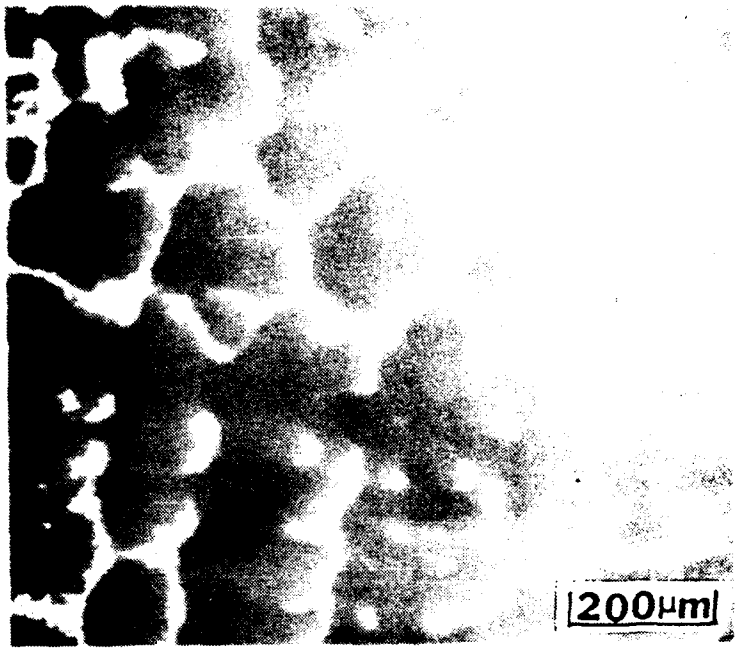

(a)

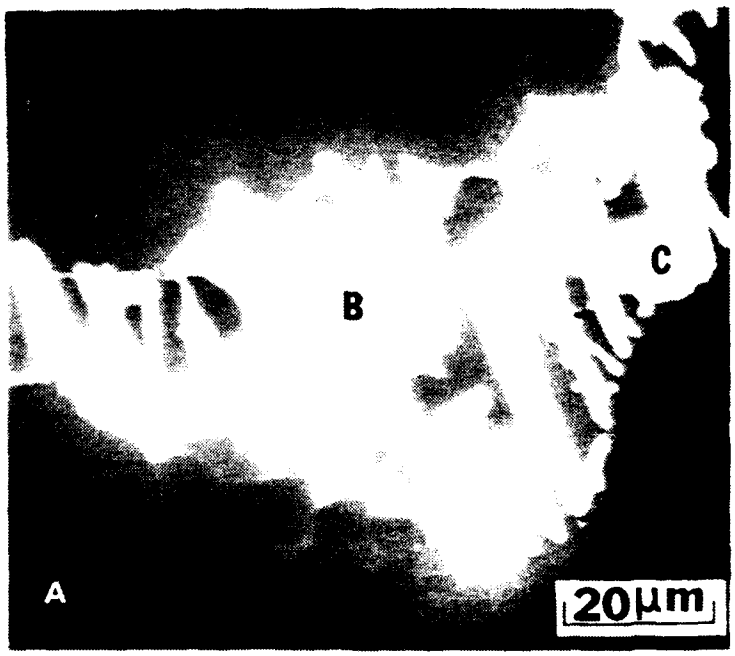

(b)

Figure 10 Scanning Electron Micrograph of Sn-214 in the As-Cast Condition. The composition of the phases labelled A, B, and C in (b) are given in Table 4.

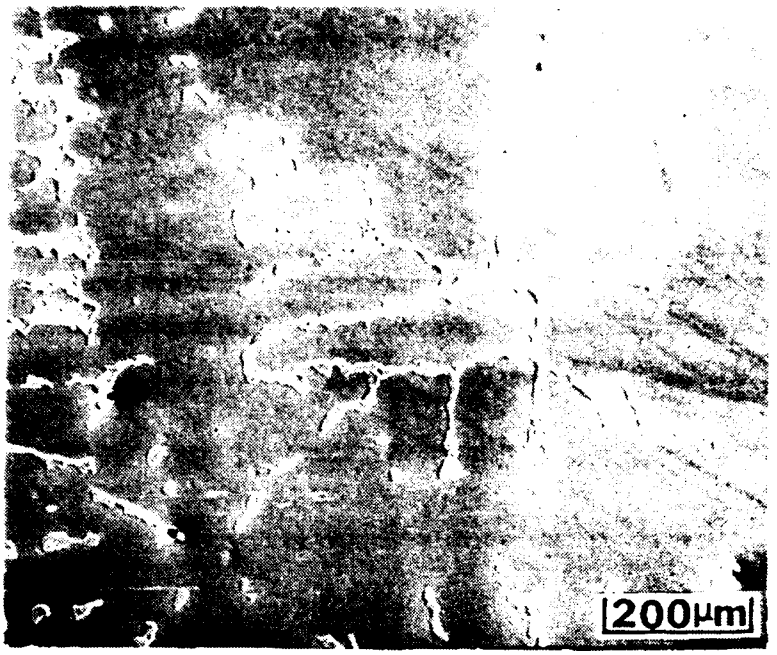

(a)

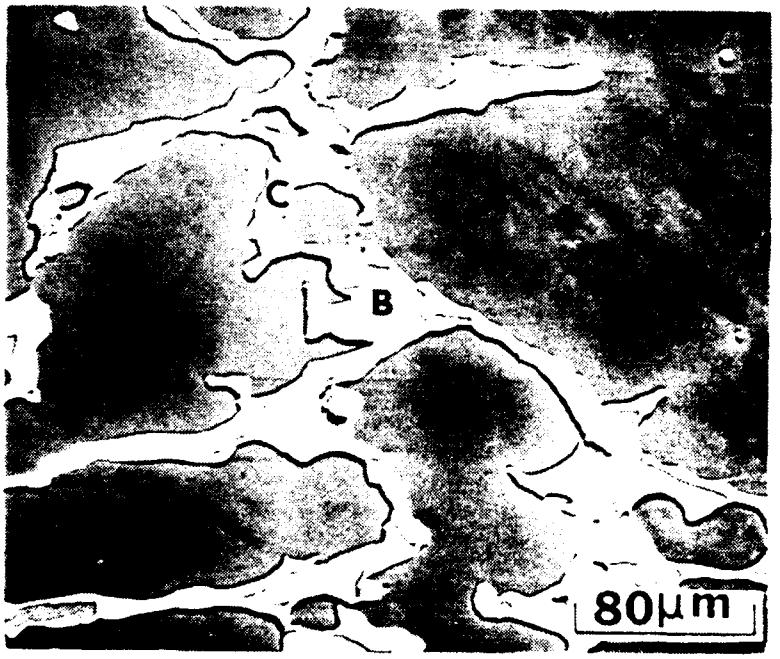

(b)

Figure 11 Scanning Electron Micrograph of Sn-214 After a Heat Treatment of 50 hours at 1339K. The composition of the phases labelled A, B, and C in (b) are given in Table 4.

(a)

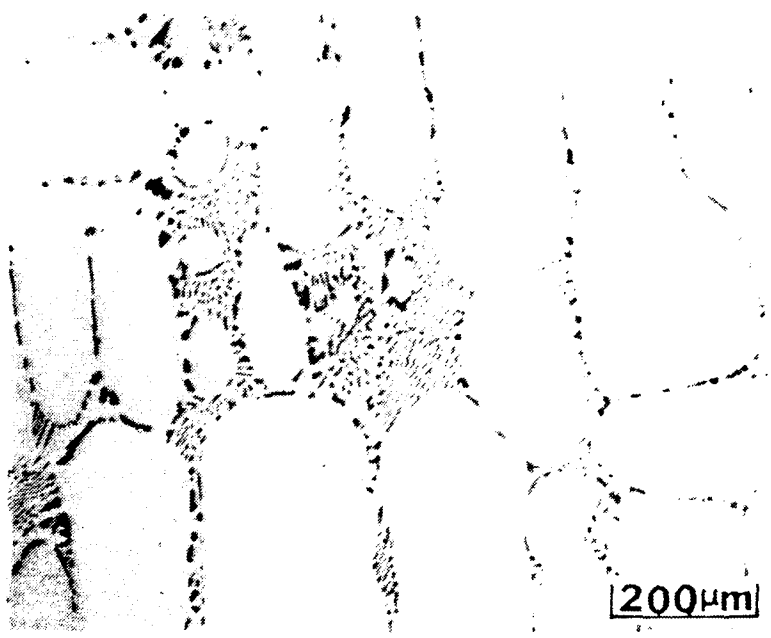

(b)

Figure 12 Microstructure of Ta-225 Single Crystal: (a) As-Cast, and (b) After 100 hours at 1477K. The dark phase is NiAl.

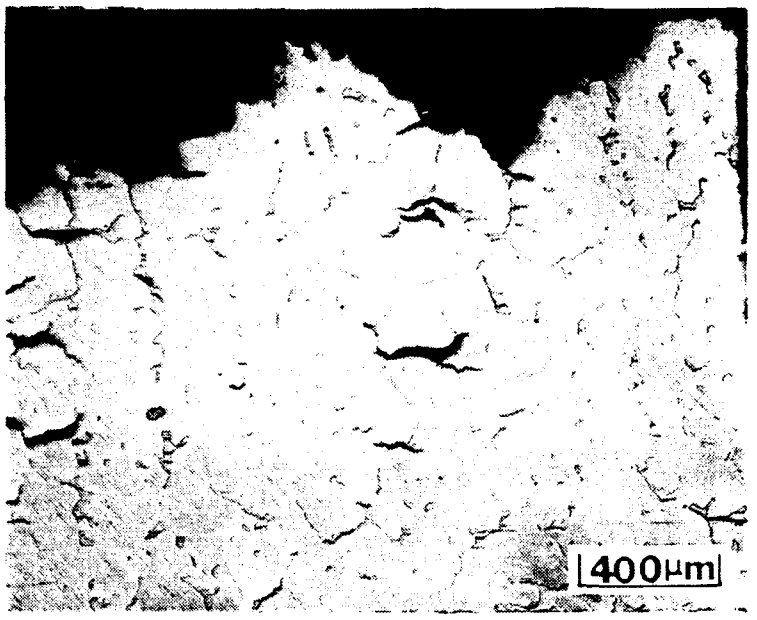

(a)

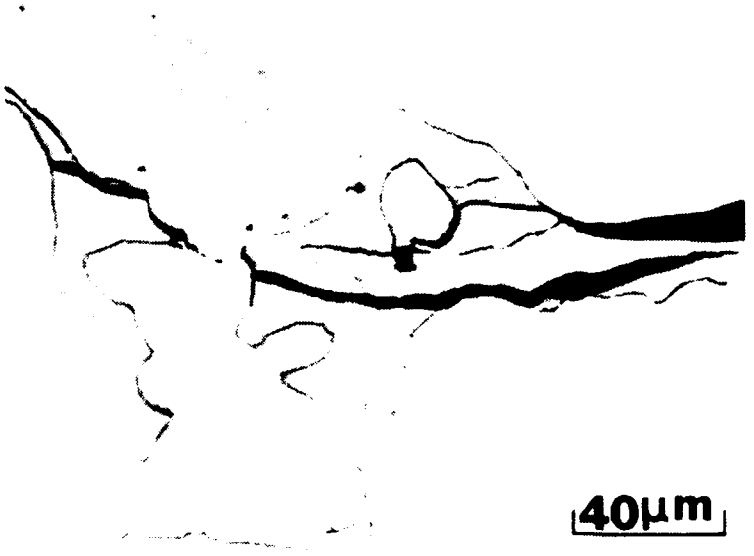

(b)

Figure 13 (a) Appearance of Fracture in Sn-204 Tested along <123> at 293K; (b) Premature Fractures in the Tin-Modified Alloy were Caused by Cracking of the Secondary Intermetallic Phases

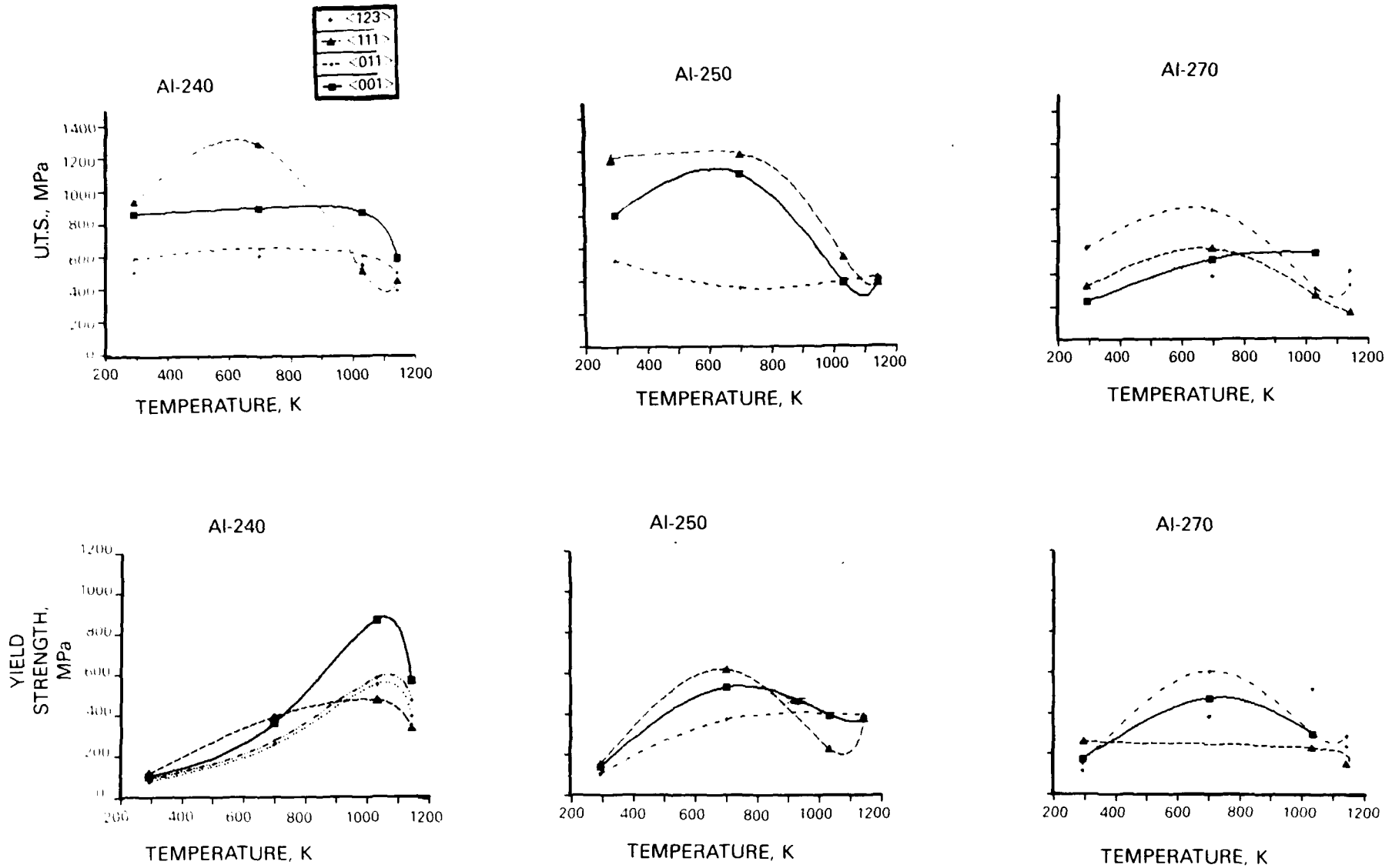

Figure 14 Tensile Yield and Ultimate Strength Versus Temperature Curves for Binary Ni_3Al Alloys Tested Along <001>, <011>, <111>, and <123> Directions

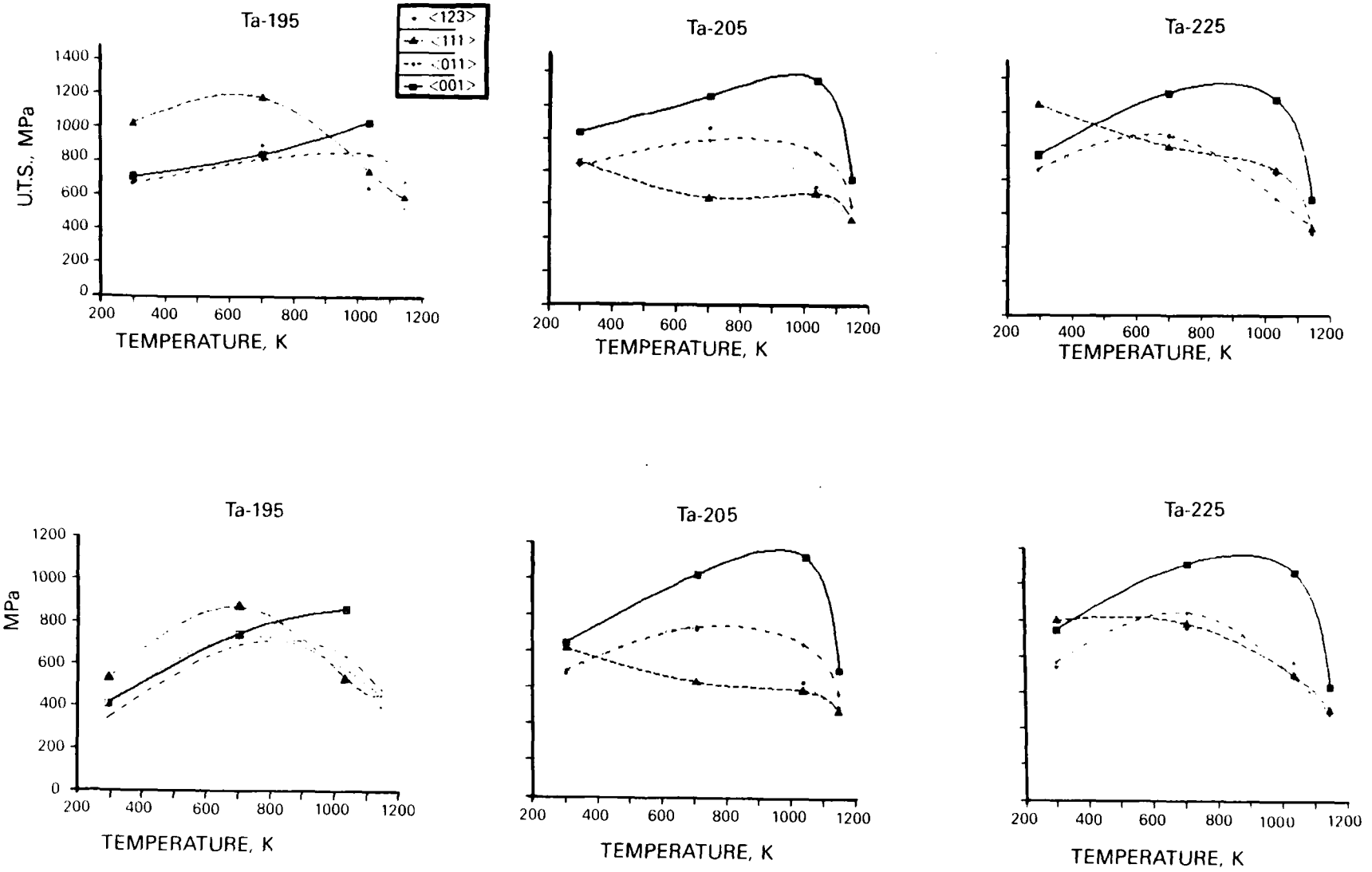

Figure 15 Tensile Yield and Ultimate Strength Versus Temperature Curves for Tantalum-Modified Ni_3Al Alloys Tested Along <001>, <011>, <111>, and <123> Directions

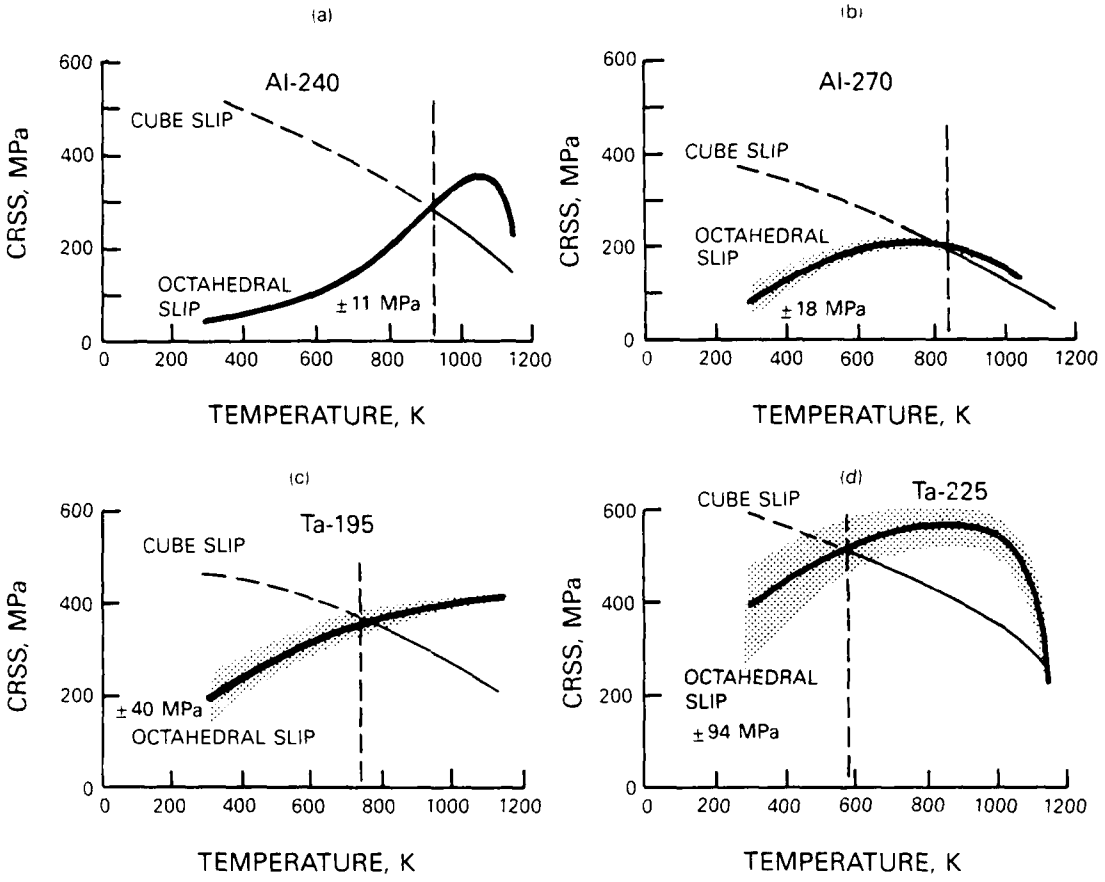

Figure 16 Comparison of Deduced CRSS Versus Temperature for Octahedral and Cube Slip Systems for: (a) Binary Al-240, (b) Binary Al-270, (c) Ternary Ta-195, and (d) Ternary Ta-225 Alloys

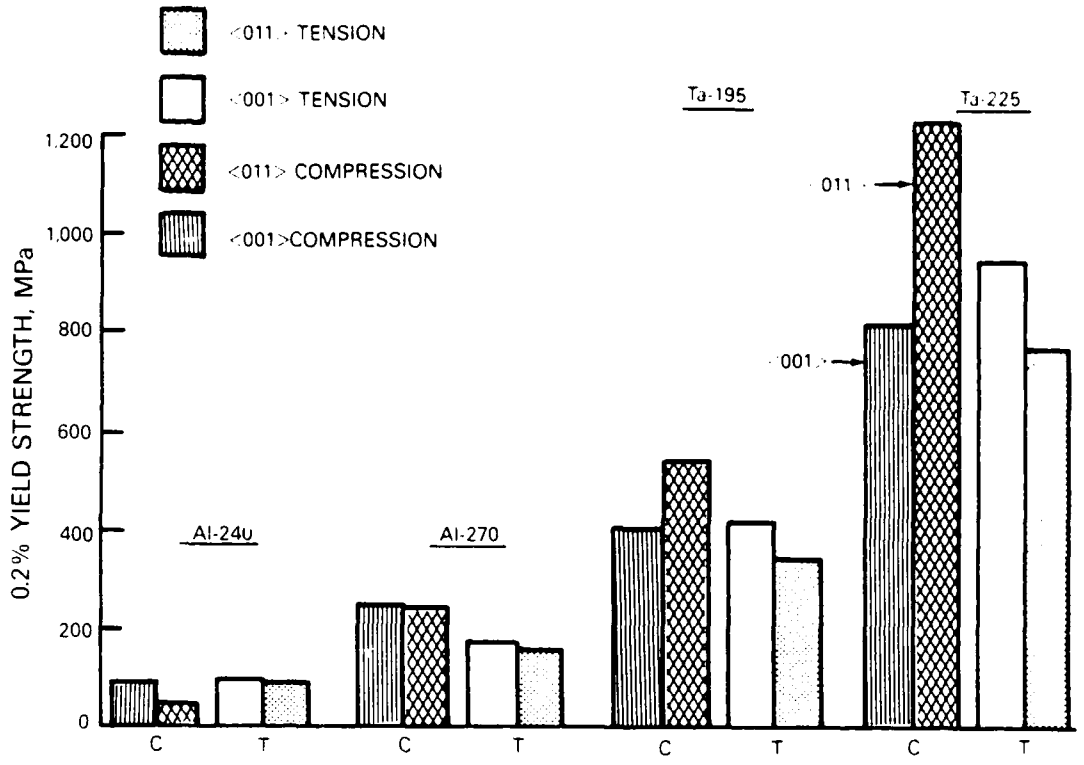

Figure 17 Comparison of Tension/Compression Asymmetry of <001> and <011> Orientations for Binary Alloys Al-240 and Al-270 and for Ternary Alloys Ta-195 and Ta-225 (C = Compression; T = Tension)

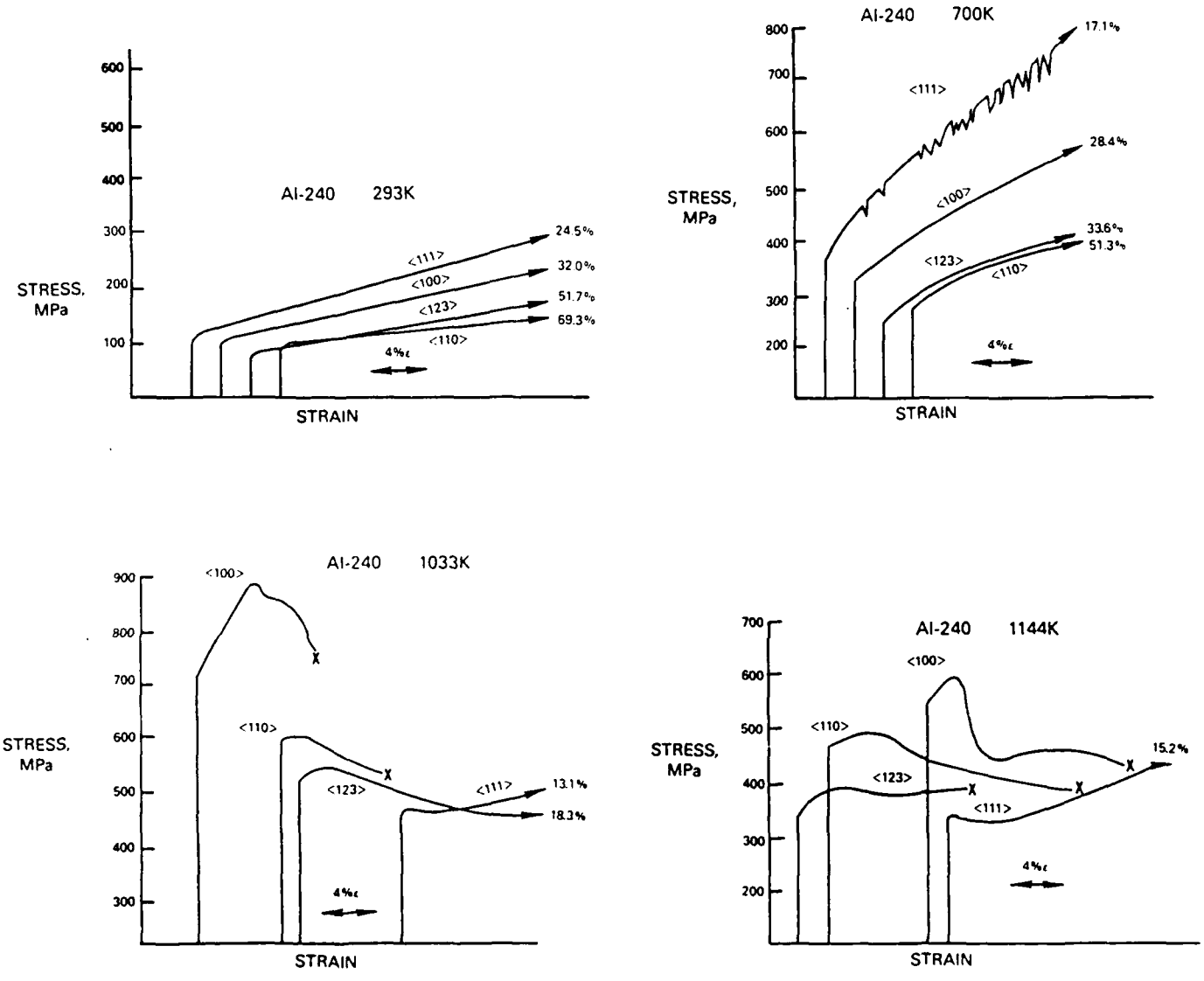

Figure 18 Tensile Stress-Strain Curves of Al-240 Tested Along <001>, <011>, <111>, and <123> Axes at 293, 700, 1033, and 1144K

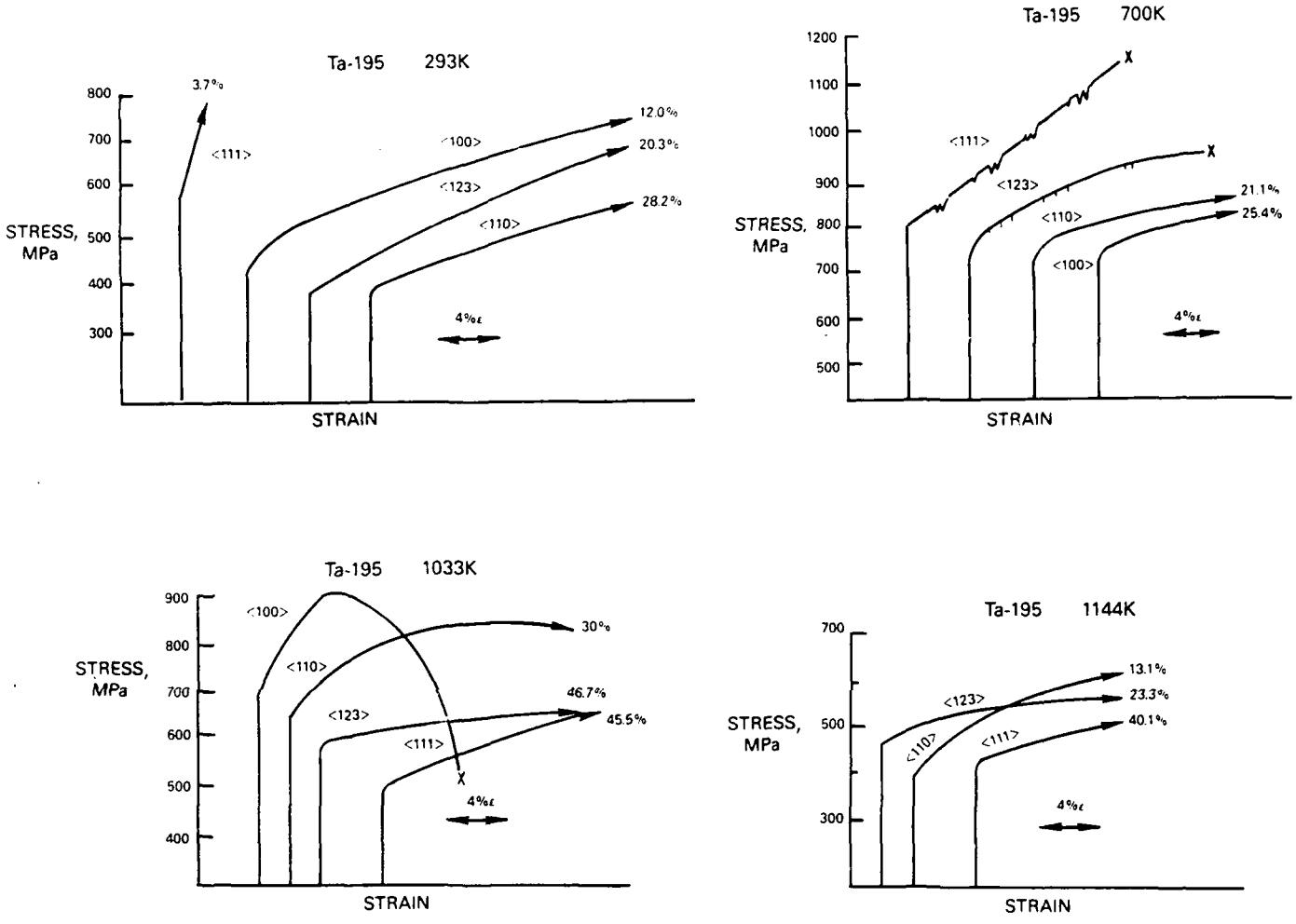

Figure 19 Tensile Stress-Strain Curves of Ta-195 Tested Along <001>, <011>, <111>, and <123> Axes at 293, 700, 1033, and 1144K

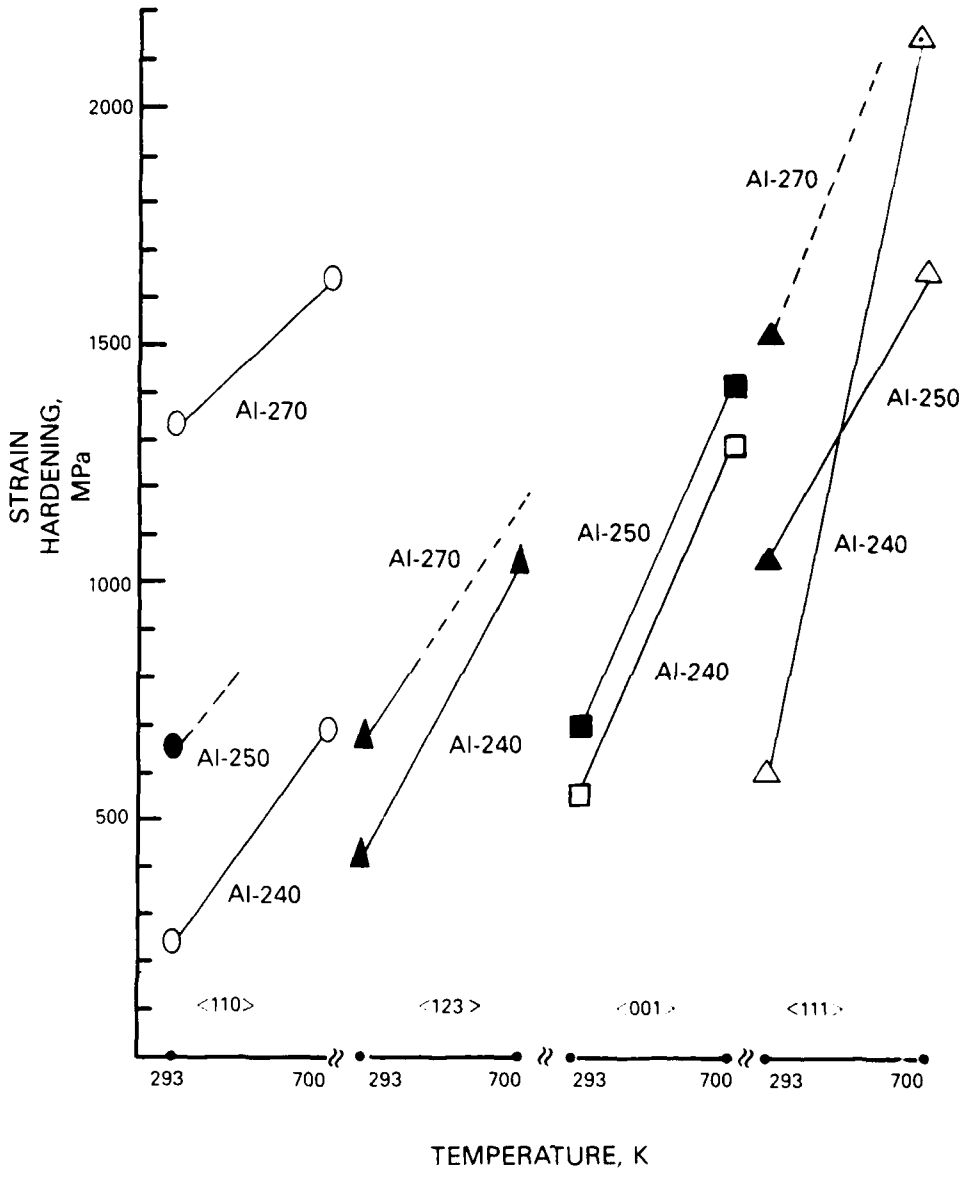

Figure 20 Tensile Strain Hardening in Binary Ni_3Al Alloys at 293 and 700K

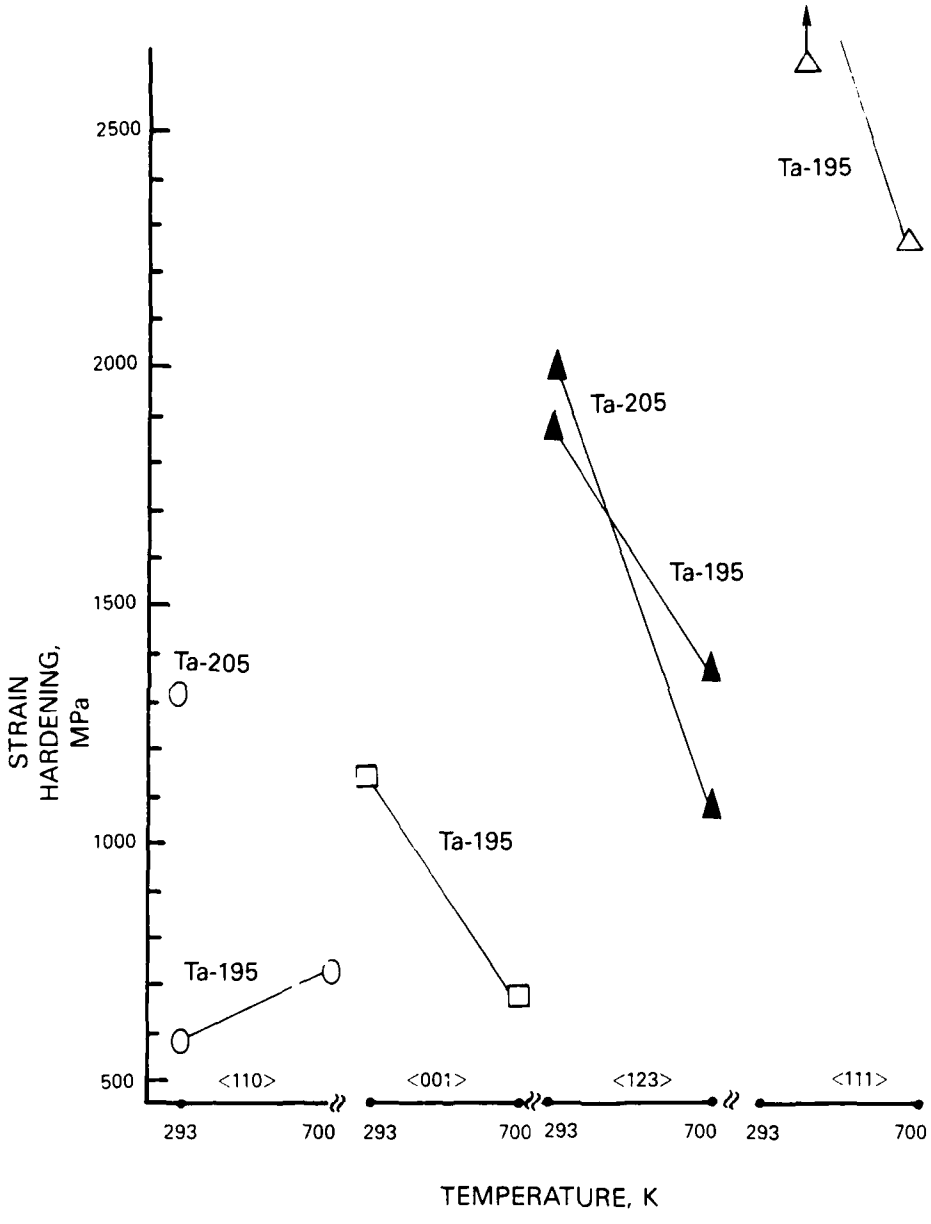

Figure 21 Tensile Strain Hardening in Tantalum-Modified Ni_3Al Alloys at 293 and 700K

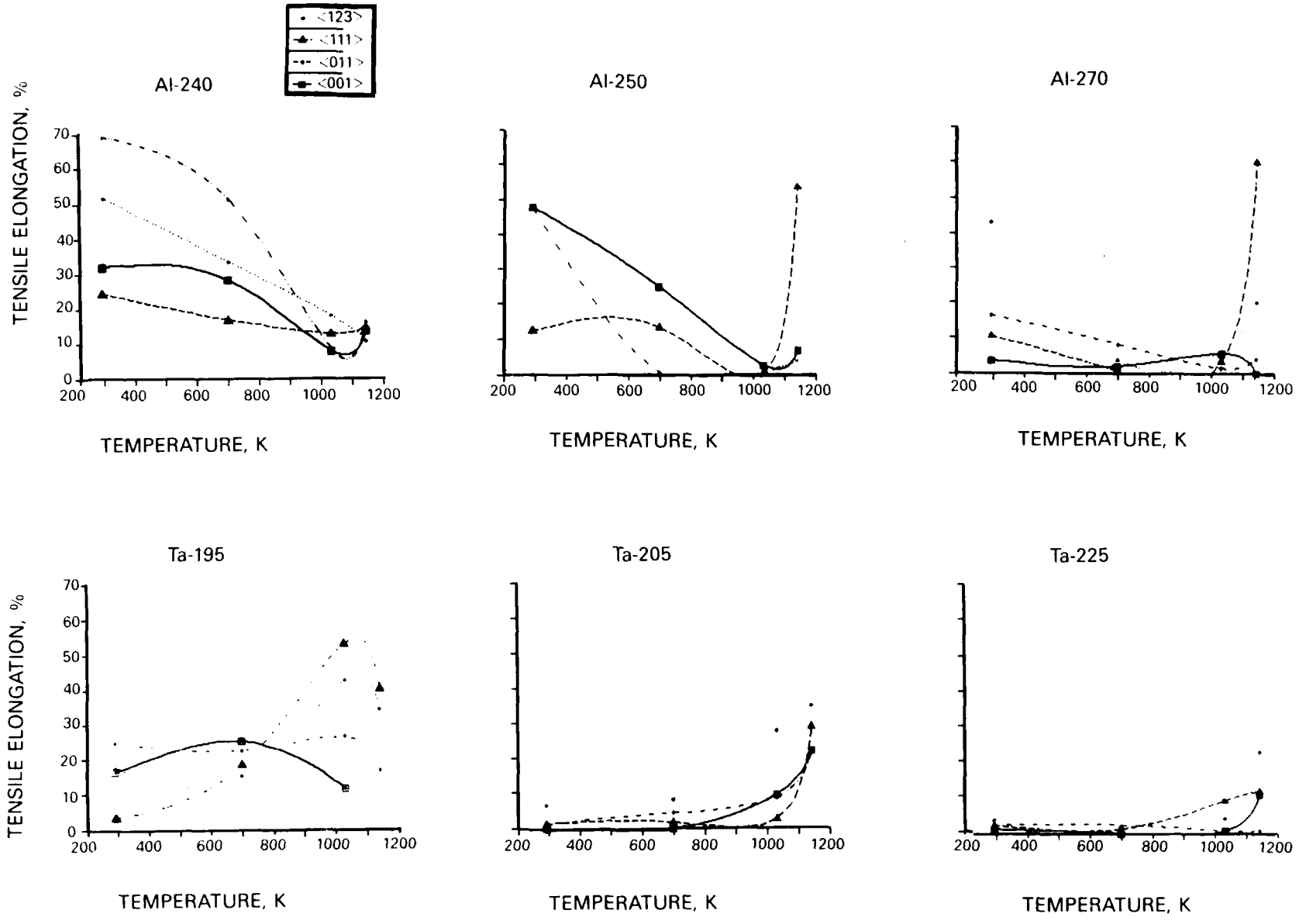

Figure 22 Tensile Elongation Versus Temperature Curves for the Binary and Tantalum-Modified Ternary Alloys Tested Along <001>, <011>, <111>, and <123> Strain Axes

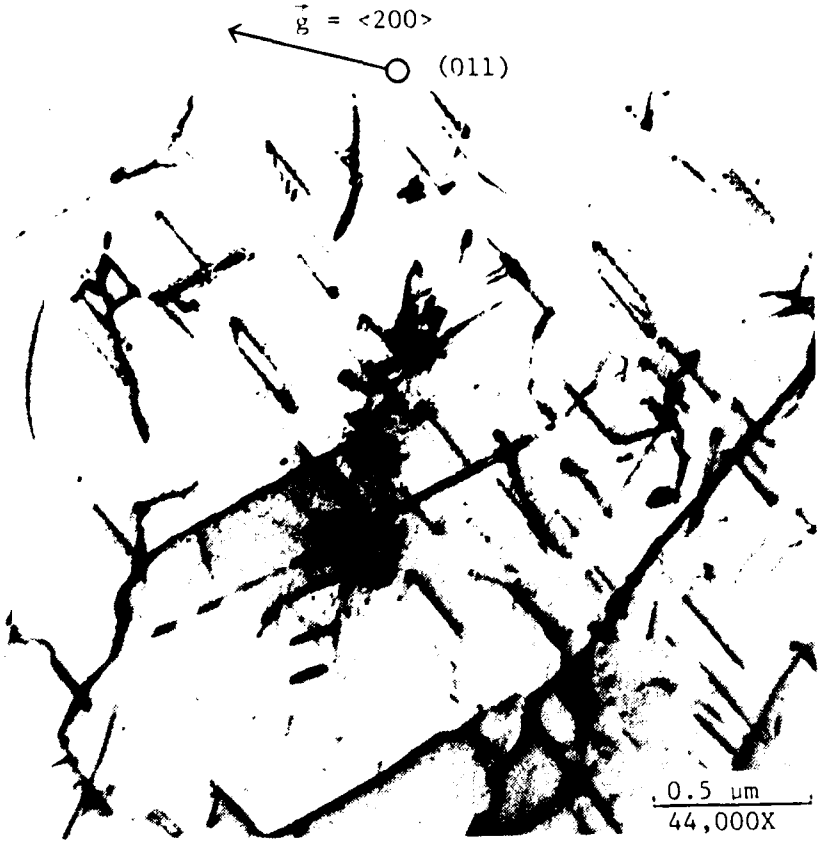

Figure 23 Dislocation Structures in Al-250 Strained Along <111> at 1144K Showing Two Sets of Screw Dislocations Bounding APB on Cube (010) Planes with Burgers Vectors of a/2<10$\bar{1}$> and a/2<101>

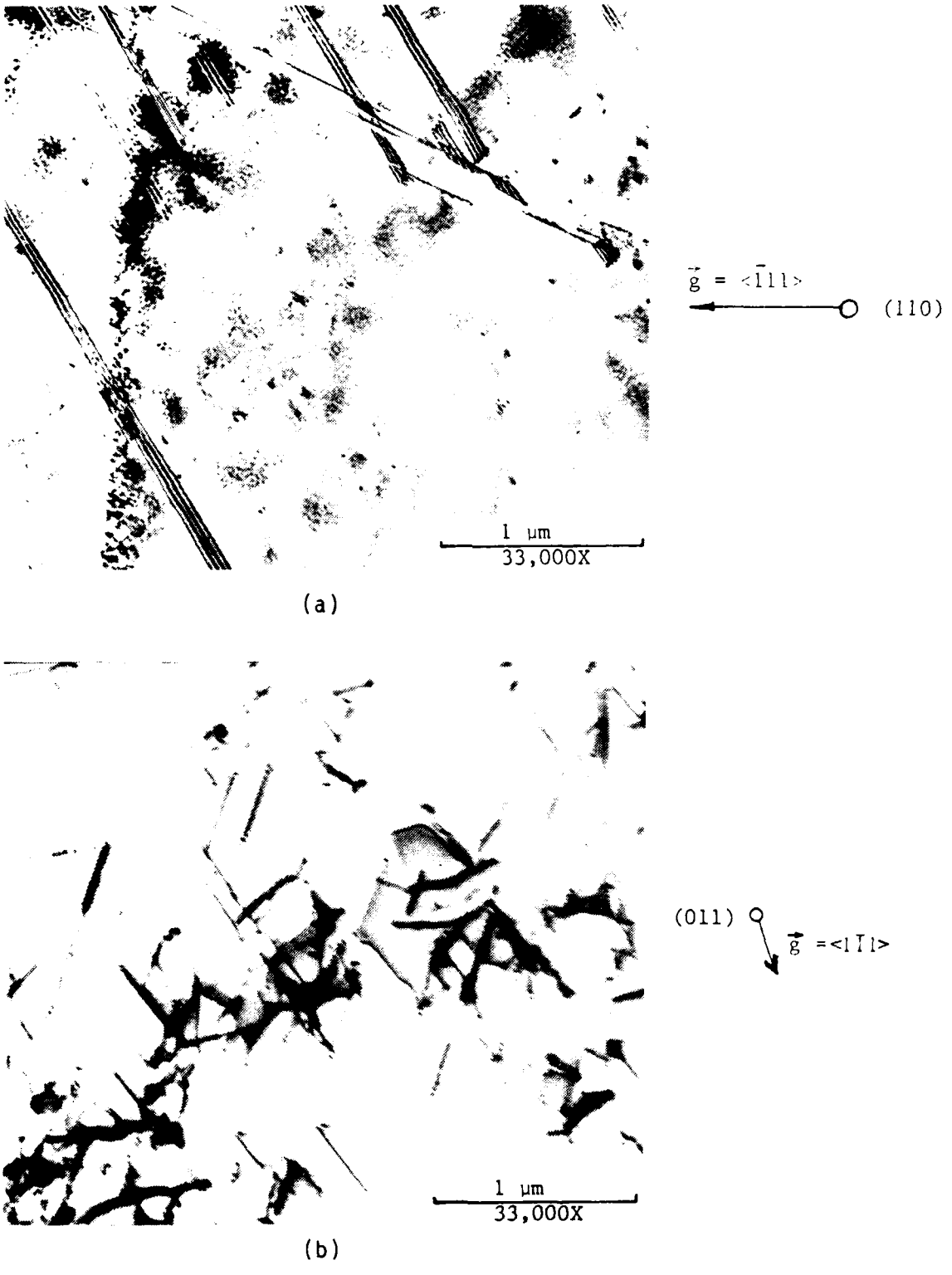

Figure 24 (a) Superlattice Intrinsic Stacking Faults, and (b) Dislocations in Al-240 Strained Along <111> to 4% at 293K (see text for description)

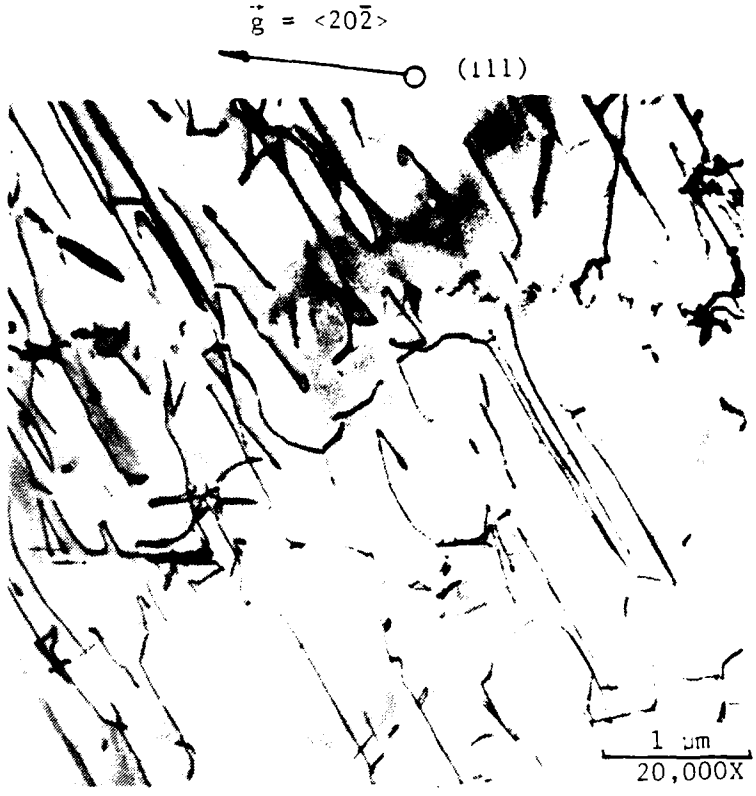

Figure 25 Dislocation Structure in Al-240 Strained Along <123> to 4% at 1033K Showing APB-Coupled Screw Dislocations with Burgers Vector a/2<$\bar{1}$10>

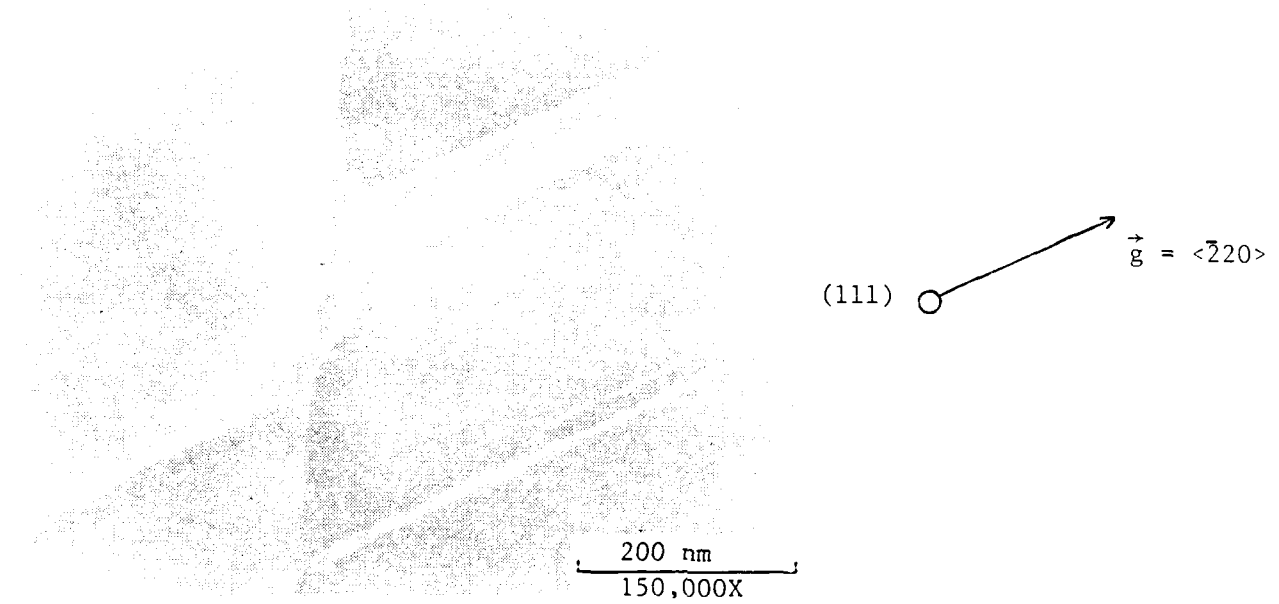

(a)

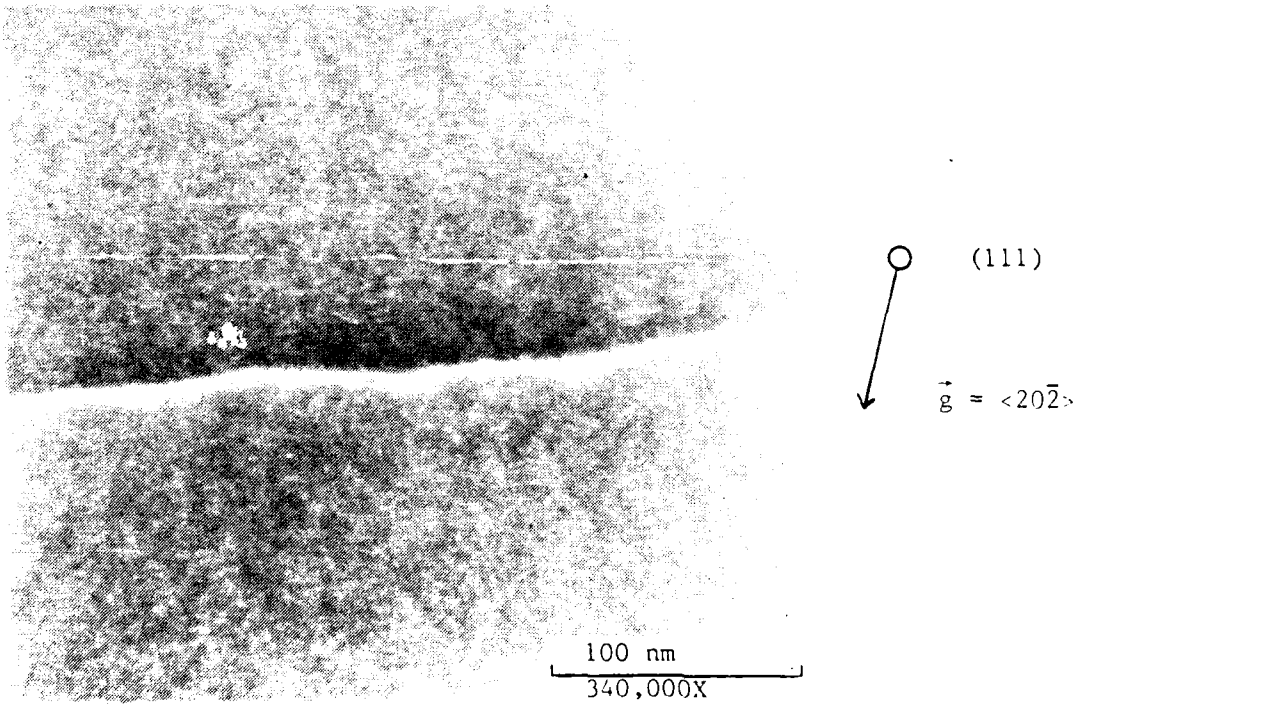

(b)

Figure 26 Spacing of APB Coupled-Dislocation Pairs in: (a) 5.0 nm in Al-240, and (b) 3.5 nm in Al-270. Dislocations imaged using weak beam dark field technique ($\vec{g}$, $3\vec{g}$) on (111) plane with $\vec{g}$ = $\bar{2}$20. Both alloys were strained along <123> to 4% at 1033K.

Figure 27 Dislocation Structure in Al-270 Strained Along <$\bar{1}$23> to 4% Strain at 1033K Showing APB-Coupled Screw Dislocations on the Cube Plane

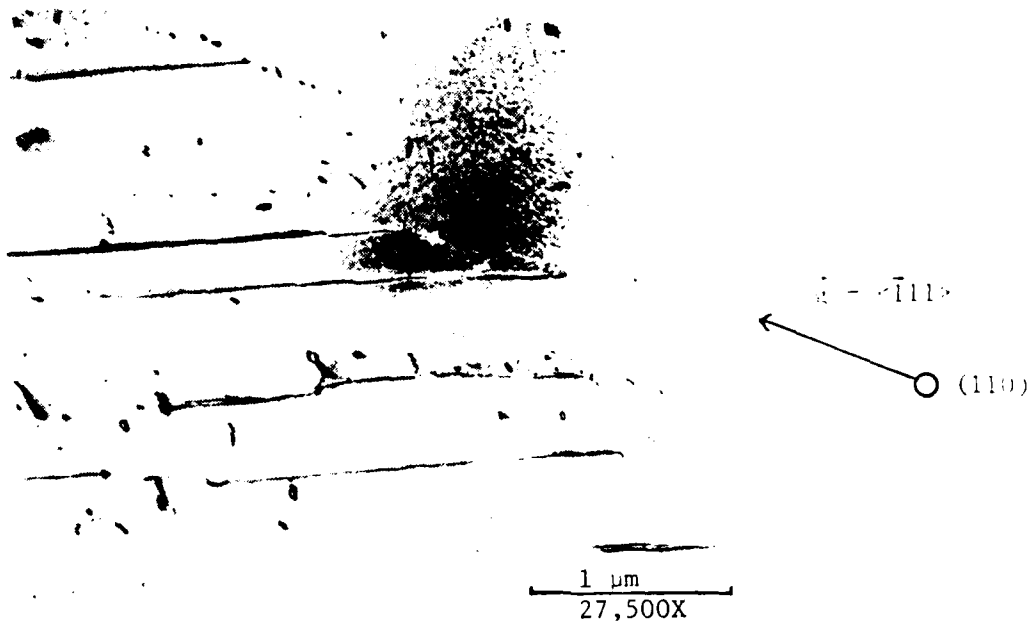

(a)

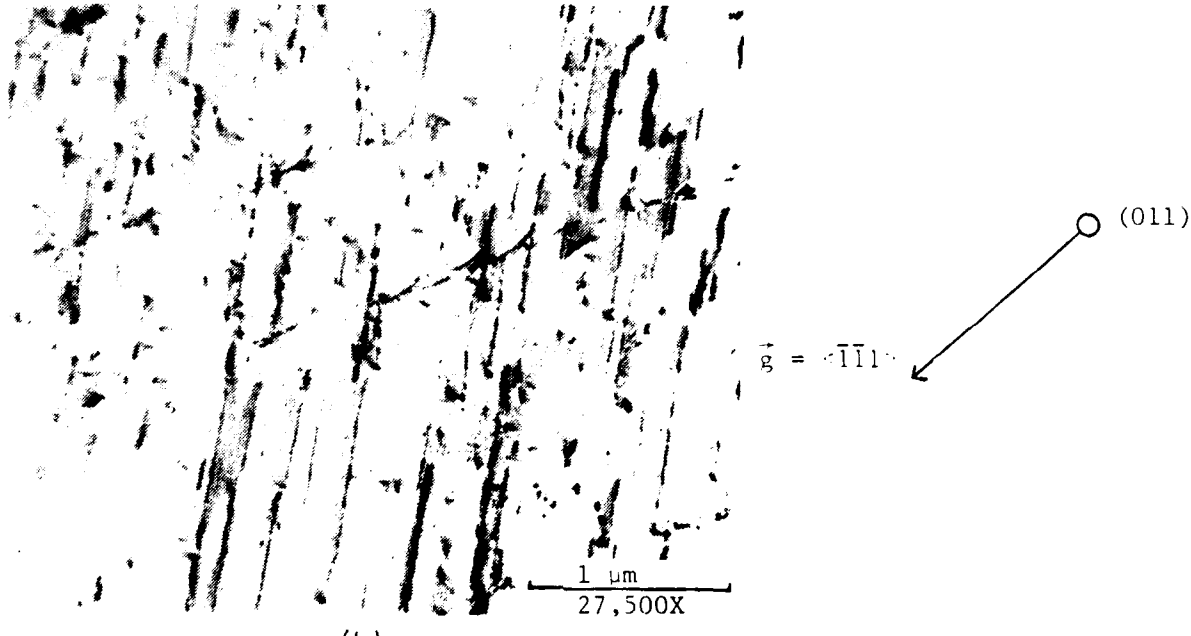

(b)

Figure 28 Dislocation Structure in Ta-195 Strained Along <123> to 4% Strain at: (a) 293K Showing APB-Coupled Screw Dislocations on (111) Plane, and (b) 1033K Showing APB-Coupled Screw Dislocations on (100) Plane

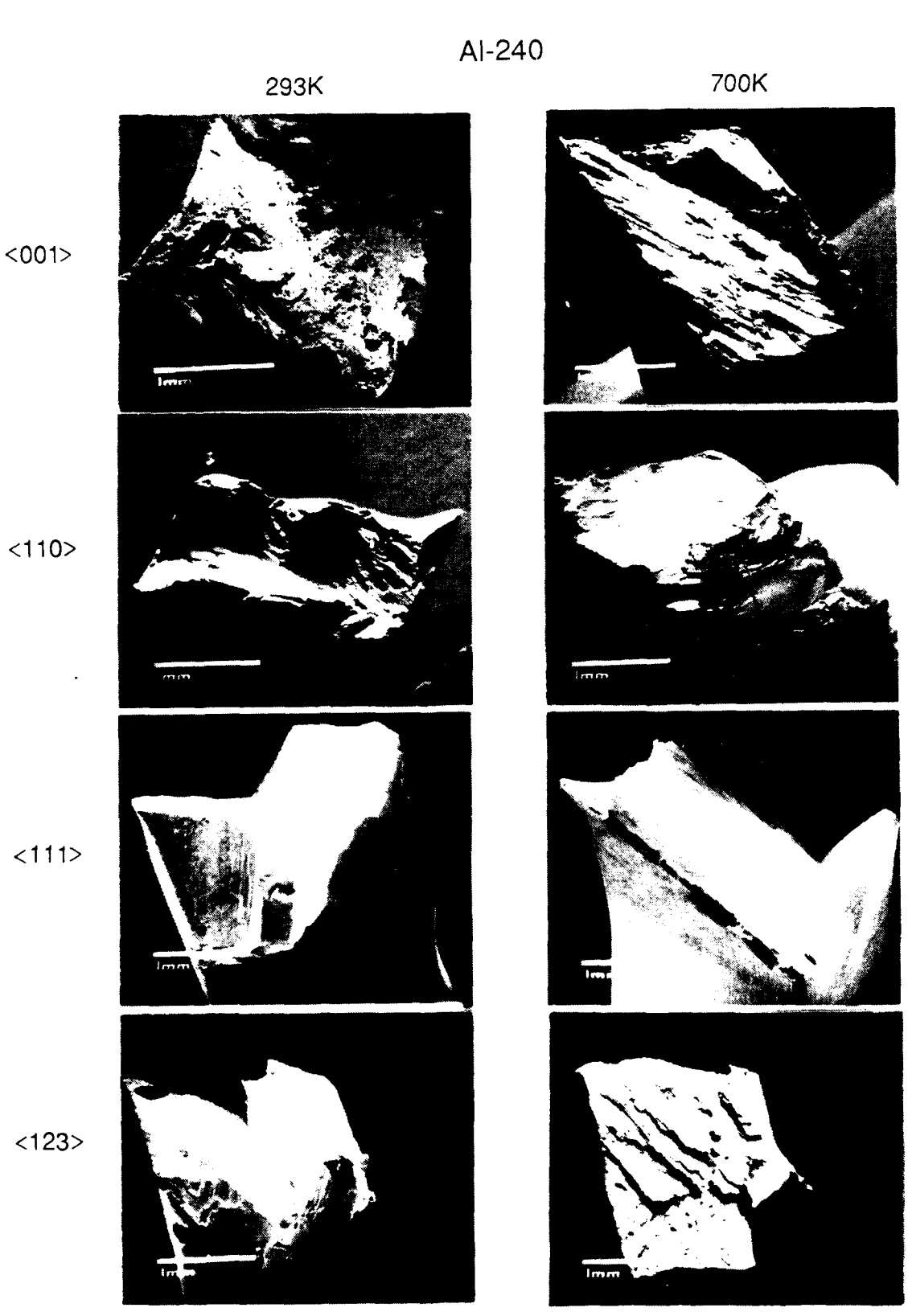

Figure 29 Appearance of Fracture Surfaces in the Binary Alloy Al-240 Resulting from Tensile Testing at 293K (left photos) and 700K (right photos). The tensile stress axes are from top to bottom <001>, <110>, <111>, and <123>.

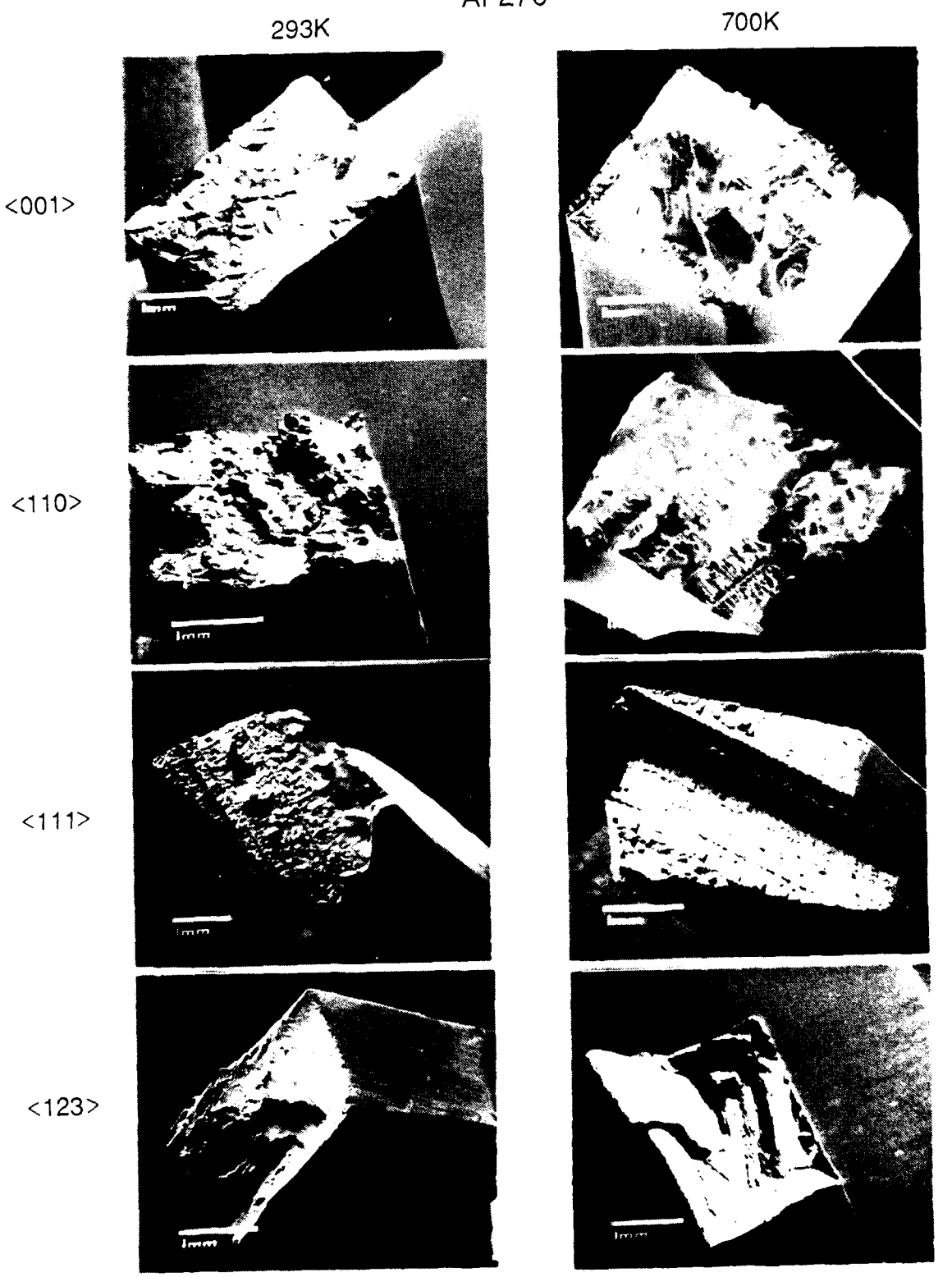

Figure 30 Appearance of Fracture Surfaces in the Binary Alloy Al-270 Resulting from Tensile Testing at 293K (left photos) and 700K (right photos). The tensile stress axes are from top to bottom <001>, <110>, <111>, and <123>.

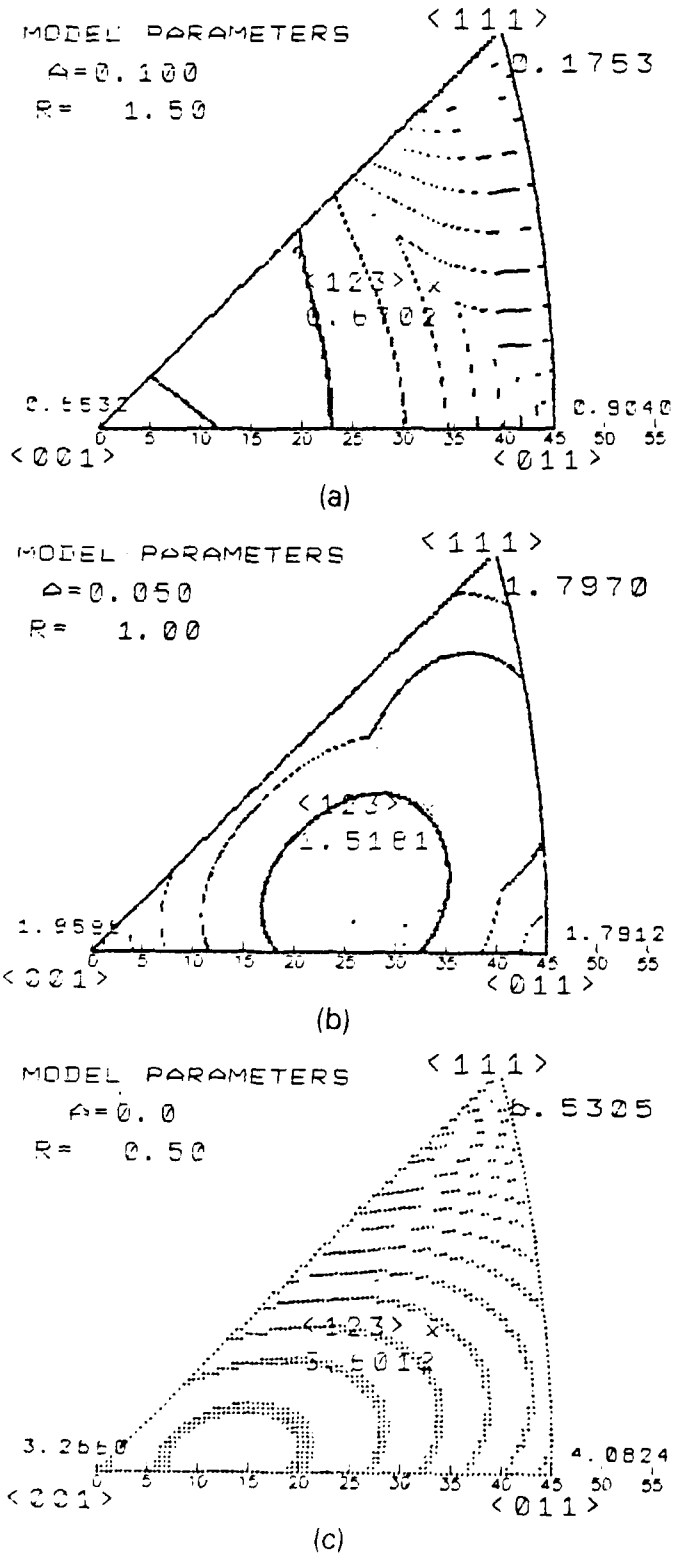

Figure 31 Model Calculations of Relative Elongation Contours within a Standard Orientation Triangle: (a) Deformation Mostly by Octahedral Slip with Strong Interaction, (b) Equal Participation of Both Cube and Octahedral Slip with Moderate Interaction, and (c) Deformation Dominated by Cube Slip with No Interaction

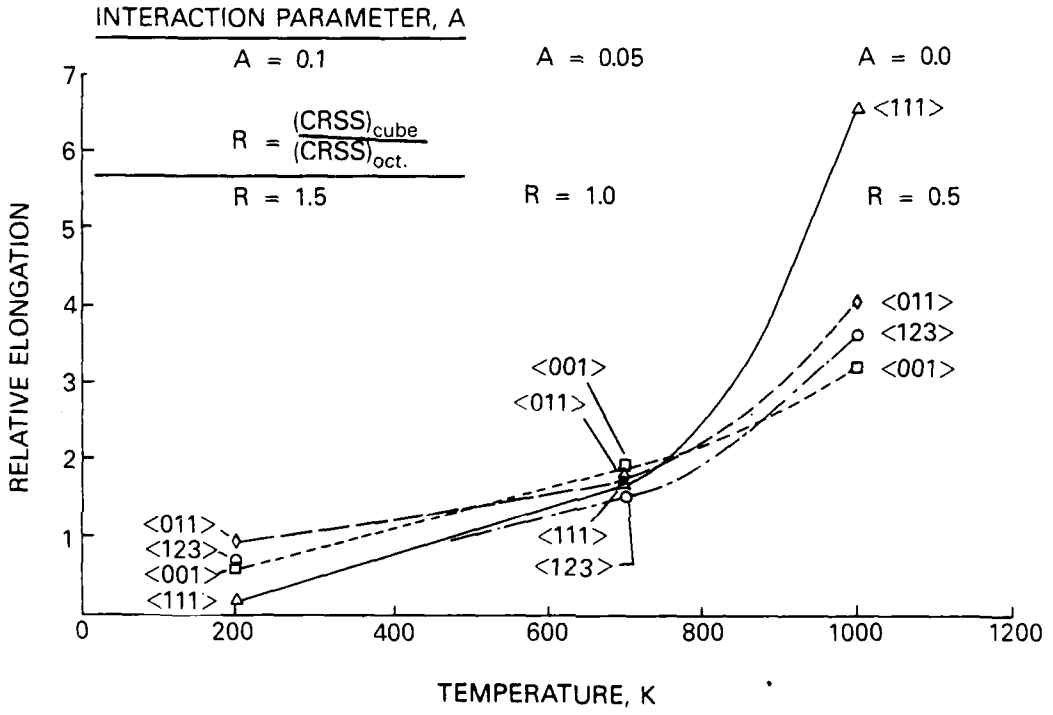

Figure 32 Model Calculation of Orientation and Temperature Dependence of Relative Elongation for Ternary Alloy Ta-195

END

DATE

FILMED

DTIC

9-88